General Disclaimer

One or more of the Following Statements may affect this Document

- This document has been reproduced from the best copy furnished by the organizational source. It is being released in the interest of making available as much information as possible.

- This document may contain data, which exceeds the sheet parameters. It was furnished in this condition by the organizational source and is the best copy available.

- This document may contain tone-on-tone or color graphs, charts and/or pictures, which have been reproduced in black and white.

- This document is paginated as submitted by the original source.

- Portions of this document are not fully legible due to the historical nature of some of the material. However, it is the best reproduction available from the original submission.

Produced by the NASA Center for Aerospace Information (CASI)

UNCLASSIFIED

FINAL REPORT

WIND VELOCITY MEASUREMENTS

R67-4548

30 November 1967

RAYTHEON

RAYTHEON COMPANY

SPACE AND INFORMATION SYSTEMS DIVISION

N69-26721

(ACCESSION NUMBER) 83 (PAGES)

(THRU) 1

(CODE) 14

CR 101108 (NASA CR OR TMX OR AD NUMBER)

(CATEGORY)

FACILITY FORM 602

RAYTHEON COMPANY

SPACE AND INFORMATION SYSTEMS DIVISION

FINAL REPORT

WIND VELOCITY MEASUREMENTS

R67-4548

30 November 1967

Prepared for

GEORGE C. MARSHALL SPACE FLIGHT CENTER

NASA

Huntsville, Alabama

Under

Contract No. NAS8-20413

Prepared by

RAYTHEON COMPANY

SPACE AND INFORMATION SYSTEMS DIVISION

Sudbury, Massachusetts

FOREWORD

This report has been prepared by the Raytheon Company, Space and Information Systems Division, Sudbury, Massachusetts, under NASA Contract NAS8-20413. The work is administered under the direction of the George C. Marshall Space Flight Center, Huntsville, Alabama. Administration of this program is under Mr. R. M. Huffaker, Project Engineer for the Aero-astrodynamics Laboratory, Aerophysics Division.

For the Raytheon Company during this program, Mr. A. Jelalian was Project Manager for the Applied Physics Laboratory, which is directed by Mr. I. Goldstein. Chief contributors to the investigation are:

E. Chouinard
I. Goldstein
C. Harris
Dr. F. Horrigan
A. Hurkamp
A. Jelalian
Dr. W. Keene (Experimental Team Leader)
Dr. P. Miles
R. Schaaf
R. Seavey
Dr. C. Sonnenschein (Theoretical Team Leader)

TABLE OF CONTENTS

Section		Page
1.0	INTRODUCTION	1-1
	1.1 Program Objectives	1-1
	1.2 Program Summary	1-1
	1.3 Conclusions	1-2
2.0	SYSTEMS STUDIES	2-1
	2.1 Introduction	2-1
	2.2 Parametric Analysis	2-1
	2.3 Optical Analysis	2-5
	2.4 Far Field Diffuse Target Losses	2-9
	2.4.1 Introduction	2-9
	2.4.2 Target Characteristics - Incoherent Scattering	2-9
	2.4.3 The Model	2-10
	2.4.4 Gaussian Output	2-20
	2.5 Comparison of Diffuse Target Analyses	2-23
3.0	ATMOSPHERIC SCATTERING	3-1
	3.1 Introduction.	3-1
	3.2 Scattering Theory	3-2
	3.3 Rayleigh Scattering Theory	3-3
	3.4 Mie Scattering Theory	3-6
	3.5 Aerosol Scattering	3-8
	3.6 Particle Size Distribution of Atmospheric Aerosol	3-10
4.0	EXPERIMENTATION	4-1
	4.1 Doppler Returns from Leaves, Rain, Haze, and Smoke	4-1
	4.2 Heterodyne Detection Experiments	4-3
	4.2.1 Heterodyne Measurements	4-13

TABLE OF CONTENTS (Continued)

Section			Page
	4.2.2	Characteristic Curves	4-14
	4.2.3	Coherence Areas	4-22
	4.2.4	Wheel Reflectivity Measurements . .	4-24
	4.2.5	Noise Measurements	4-28
	4.2.6	Wind Tunnel Experiments	4-29
4.3	Summary		4-37

ILLUSTRATIONS

Figure		Page
2-1	Configuration Used in the Calculation of Diffuse Target Losses	2-12
2-2	Heterodyne Signal from Diffuse Target	2-17
2-3	Relative Loss of Signal Coherence	2-21
3-1	Scattering Efficiency versus Size Parameter	3-7
4-1	Doppler Returns from Wind Blown Leaves at 500-Foot Range	4-4
4-2	Doppler Returns from Moderate Rain	4-4
4-3	Doppler Returns from Haze on a Humid Day	4-5
4-4	Doppler Returns from Haze on a Humid Day	4-5
4-5	Doppler Returns from Haze on a Humid Day	4-6
4-6	Doppler Returns from Haze on a Humid Day	4-6
4-7	Doppler Returns from Haze on a Humid Day	4-7
4-8	Doppler Returns from Haze on a Humid Day	4-7
4-9	Doppler Returns from Wind-Blown Smoke at 15-Foot Range	4-8
4-10	Doppler Returns from Smoke Which Had Dissipated	4-8
4-11	Smoke Generator Turned Off and Smoke has Mostly Dissipated	4-9
4-12	Doppler Returns from Smoke at 15-Foot Range	4-9
4-13	Doppler Returns from Smoke at 15-Foot Range	4-10
4-14	Smoke Generator Setup at 15-Foot Range	4-10
4-15	Doppler Returns from Wind-Blown Smoke at 200-Foot Range	4-11
4-16	Doppler Returns from Wind-Blown Smoke at 200-Foot Range	4-11
4-17	Smoke Generator at 200-Foot Range	4-12
4-18	Smoke Generator at 200-Foot Range	4-12

ILLUSTRATIONS (Continued)

Figure		Page
4-19	Bias Voltage vs Incident Power at 10.6 Microns for Constant Bias Current	4-15
4-20	$\Delta v/\Delta p$ at Constant Bias Current vs Incident Power at 10.6 Microns	4-16
4-21	Bias Current vs Incident Power for Constant Bias Voltage	4-17
4-22	$\Delta I/\Delta P$ at Constant Bias Voltage vs Incident Power.	4-18
4-23	Bias Voltage vs Bias Current for Constant Incident Power	4-19
4-24	$\Delta v/\Delta I$ at Constant Incident Power vs Bias Current.	4-20
4-25	Experimental Setup for Wheel Reflectivity Measurements	4-25
4-26	Circuit for Detector Noise Measurements	4-30
4-27	Noise Spectrum of the Detector for Various Bias Currents with Local Oscillator Off	4-31
4-28	Noise Spectrum of the Detector for Various Bias Currents with Local Oscillator Power of 11.5 Milliwatts	4-31
4-29	Experimental Arrangement for Wind Tunnel Tests .	4-34
4-30	Wind Tunnel	4-35
4-31	Doppler Returns from High Smoke Concentration in Wind Tunnel	4-36
4-32	Doppler Returns from Very Low Smoke Concentration in Wind Tunnel 10 Minutes after Smoke was Turned Off	4-36
4-33	Doppler Returns from Wind Tunnel	4-38
4-34	Doppler Returns from Wind Tunnel	4-38
4-35	Doppler Returns from Smoke in Wind Tunnel	4-39
4-36	Doppler Returns from Smoke in Wind Tunnel	4-39
4-37	Doppler Returns from Smoke in Wind Tunnel	4-40

1.0 INTRODUCTION

1.1 Program Objectives

This document constitutes the final report for the Wind Velocity Measurement phase of the Doppler Flowmeter Contract Number NAS 8-20413. The objectives of this program are threefold:

1. To demonstrate the feasibility of remotely measuring the velocity of both clear and contaminated air.
2. To perform system analyses of both short and long range remote optical heterodyne wind velocity measurement systems.
3. To investigate the scattering properties of the atmosphere.

1.2 Program Summary

The program effort consisted of an analysis of short and long range Optical Doppler Wind Velocity and Turbulence measurement systems which is included in Section 2, along with a rigorous analysis of the coherence area associated with diffuse targets. Analyses indicated that this source of loss would predominate and therefore a detailed study was conducted. The results indicate that if the transmitter and receiver optics are matched, a diffuse target loss of the order of 3.5 db is expected in the far field of both transmitter and receiver.

The determination of the atmospheric target cross-section is essential to the practical measurement of atmospheric effects with a Doppler system. Due to the limited funding of this program an answer to this could not be fully obtained; hence a theoretical analysis indicating additional requirements was conducted and is presented in Section 3. The discussion involves

the distinction between Rayleigh and Mie scattering. Results of the literature search conducted to determine particle size distribution and particle number density illustrated the total lack of measured data at the 10.6 micron wavelength and dramatized the need for such measurements in order to predict the atmospheric target cross-section.

Section 4 discusses the experimental measurement program. Results of atmospheric tests indicated that returns were obtained for clear air, smoke, haze, rain and leaves although the system did not have collecting optics and suffered 25 db non-optimum system loss. This loss appears to be caused by the optical heterodyning efficiency being lower than anticipated. In order to resolve this 25 db discrepancy between theoretical predictions and actual measurement the experimental program focused on a detailed analysis of the 10.6 μ Cu:Ge detector. Experiments were performed to:

(1) determine the characteristics curves of the detector

(2) verify the heterodyne equation

(3) measure the noise sources

(4) determine coherence areas

At the conclusion of the contract these measurements were still continuing and an indication of optimum detector operating conditions was evolving.

1.3 Conclusions

At the end of this program it is possible to draw some conclusions concerning the feasibility of constructing a remote Optical Doppler Wind Velocity System. The success in obtaining returns from targets such as haze, rain, and smoke with a non-optimum system leave little doubt that such a measurement system can be built. Continuing studies will make it possible to operate the detector at best biasing conditions, which hopefully will recover much of the missing 25 db. Similarly, a

stabilized laser will make measurements easier, more reliable, and more noise-free. The analysis contained in Section 2 on diffuse target losses has shown that previous estimates of this number were exceedingly conservative and that diffuse target loss in the far field may prove to have little significance.

At this point expectations for future Remote Wind Velocity Measurement Systems are quite optimistic.

2.0 SYSTEMS STUDIES

2.1 Introduction

The performance of any system depends upon many factors. One of the most significant considerations, however, must be the system signal-to-noise ratio. In this section of the report this factor will be analyzed, and the performance of a lossless system will be discussed. In this connection, the optimal system design will be shown to depend upon range and wind velocity. At short range, a CW optical heterodyne Doppler detection system is recommended, while at longer ranges a pulsed Doppler heterodyne system is more desirable.

Having studied the lossless system, one of the most significant loss factors will be treated in detail. When a signal is scattered from a diffuse target, the scattered return has less spatial coherence than the same signal scattered from a specular target. This loss of coherence gives a smaller output after heterodyning than an identical specular return. This difference is called the diffuse target loss.

The diffuse target loss has been analyzed by two different techniques in the course of this program. The traditional optical approach will be treated first. This method involves several assumptions whose validity is range dependent, so significant errors may result in the far field. For this reason a rigorous analysis valid only in the far field is presented. A similar derivation is still required at shorter ranges.

2.2 Parametric Analysis

The feasibility of an optical Doppler system to remotely measure the return signal from atmospheric particles centers around the S/N equation. The S/N power at the output of the

receiver for a monochromatic source is:

$$S/N = \frac{\eta P_{sig} P_{LO}}{B h f \left[P_{LO} + P_N + P_{AMP}\right]} \qquad (2\text{-}1)$$

where:
- η = Detector Quantum Efficiency
- P_{sig} = Received Signal Power
- P_{LO} = Local Oscillator Signal Power
- P_N = Equivalent Optical Noise Power
- P_{AMP} = Equivalent Noise Figure Power of Post Detection Amplifier
- B = Electronic Bandwidth
- h = Planck's Constant
- f = Transmission Frequency

Typically, in a coherent detection process, the local oscillator power may be increased to a value such that the noise associated with it is much greater than all other noise sources. As a result of this the S/N equation becomes equal to the product of the detector quantum efficiency and the received signal power and inversely related to the electronic bandwidth, transmission frequency and Planck's constant.

Replacing the received signal power expression (P_{sig}) with its equivalent expression for an extended Lambertian target, the S/N equation may be observed to be a function of:

$$S/N = \frac{\eta P_T D_R^2 \times \beta \times L}{4 h f R^2 B} \qquad (2\text{-}2)$$

where:
- P_T = Transmitter Power
- D_R = Receiver Optics Diameter
- β = Aerosol Scattering Coefficient
- L = Length of Scattering Volume
- R = System Range

Of particular note are four parameters: 1) transmitter power (P_T), 2) electronic bandwidth (B), 3) the aerosol scattering coefficient (β), and 4) the length of the scattering volume (L). Typical system analyses usually revolve around determining the amount of transmitter energy required to perform a chosen task. However, for remote wind measurements at large distances, typically we are transmitter power limited. Referring to the electronic bandwidth and the length of the scattering volume, we now see that the interface between the turbulence and the turbulence detection system manifests itself in the interaction between the particulate matter velocity with the laser beam. Doppler shift occurs when there is a relative motion between the laser beam and a target.

The equation for the Doppler frequency shift (f_d) may be expressed as:

$$f_d = \frac{2V}{\lambda} \cos \theta \qquad (2\text{-}3)$$

where: V = Relative Velocity
λ = Transmission Wavelength
θ = Pointing Angle between Relative Velocity Vectors

Correspondingly the Doppler spectral bandwidth (Δf_d) caused by the uncertainty of wind velocity (ΔV) over the sampled volume is similarly related.

$$\Delta f_d = \frac{2\Delta V}{\lambda} \cos \theta \qquad (2\text{-}4)$$

The processing bandwidth may then be determined by the instantaneous velocity spread (ΔV) expected within the target volume. If a differential velocity spread of one meter per second occurred over the sampled volume than a 200 kHz processing bandwidth would be required at a 10.6-micron operating wavelength.

Correspondingly, for a 15 M/sec differential velocity, a three-megacycle bandwidth requirement would exist.

In most Doppler System applications the target does not assume a significant differential velocity within the beam and, therefore, the bandwidth of the returned Doppler spectrum is relatively small compared to that required in a pulse system utilizing ideal matched filter concepts. As the Doppler bandwidth requirement increases, the CW output power requirement increases correspondingly to maintain the same S/N ratio (refer to Equation (2-2)). The inherent advantage of coherent CW operation, i.e., significant power savings by narrow banding to the relatively narrow Doppler spectrum, is then reduced by the degree of bandwidth broadening caused by the differential velocity.

The Doppler bandwidth requirement for a differential wind velocity of one meter/second is of the order of 200 kHz, which is identical to that required for a matched filter where the pulse width is five microseconds. One must conclude, therefore, that for the situation discussed the average power required for a CW system would be substantially greater than the average required in a pulsed system. The use of a CW Doppler technique, therefore, appears inefficient for use in a long range system.

Because of the spectrum broadening caused by the turbulent wind velocity, a pulse type laser technique is indicated for a long range system having sufficient Doppler shift to make suitable measurements.

The choice of transmitter pulse width may be shown to directly affect:

1. Signal-to-Noise Ratio (S/N)
2. The Sampling Length (L)
3. The Velocity Resolution (Δf)

This indicates that the pulse width should be as large as possible consistent with the Doppler broadening anticipated over the in-

cremented measurement length. As this length increases the differential velocity expected would increase, and therefore, larger bandwidths would be required. Theoretically then, either a CW or a pulse heterodyne system could be used for Doppler detection of the velocity of particular matter in the atmosphere.

At very short ranges a pulse Doppler system might suffer T/R switch recovery time limitations and an insufficient number of Doppler cycles, and, therefore, a CW system would be more practical. Correspondingly, at long ranges the use of CW Doppler systems would seem impractical from the standpoint of transmitter power requirements and a pulse Doppler system would be indicated.

2.3 Optical Analysis

The signal-to-noise ratio in heterodyne detection at microwave frequencies varies as the square of the collector diameter. At optical frequencies, however, this is not the case. Rather, for very small collectors there is a quadratic behavior, while for larger collectors the signal-to-noise ratio appears to be independent of collector diameter. This effect is explained by an analysis of the coherence of the scattered signal.

Most targets scatter diffusely at optical frequencies. This means that light scattered from the target has little spatial coherence at distances close to the target, and, in fact, the target can be assumed to be a source with zero spatial coherence. The amount of spatial coherence increases as the distance from the target increases, so that at the plane of the collector, the scattered radiation has a non-zero coherence area. The degree of spatial coherence between two points in a plane normal to the radiation's propagation vector is given by:

$$\frac{2 J_1 (x)}{x} \qquad (2\text{-}5)$$

where: $x = \frac{2\pi}{\lambda} \frac{\rho}{R} D$ (2-6)

λ = wavelength of radiation
ρ = radius of target
R = distance to target
D = distance between points in plane
J_1 = Bessel function of first kind and first order

The function $2 J_1 (x)/x$ decreases monotonically from a value of 1 when $x = 0$ to a value of 0 when $x = 3.83$. Because of the mathematical complexity, it is usually assumed that only the region for which $x \leq 1$ is useful for heterodyne detection, and in this region the radiation is completely spatially coherent. For larger values of x, it is assumed that there is no spatial coherence, so the region is useless for heterodyning. (This can be seen to be a conservative assumption since $2 J_1 (1)/1 = 0.88$.)

Using this information an effective collector diameter from Equation (2-6) can be defined for $x = 1$:

$$D_{EFF} = \frac{\lambda R}{2\pi \rho} \quad (2-7)$$

or

$$D_{EFF} = \frac{.16 \lambda R}{\rho} \quad (2-8)$$

According to the above assumptions, for heterodyne detection D_{EFF} should be used in place of D_R in Equation (2-2) for the signal-to-noise ratio, so the diffuse target loss equals $(D_{EFF}/D_R)^2$. Substituting Equation (2-8),

$$\text{diffuse target loss} = \left(\frac{.16 \lambda R}{\rho D_R}\right)^2 \quad (2-9)$$

From these remarks, conclusions can be drawn that are relevant to a particular system. For a coaxial heterodyne system, where the target intercepts all of the transmitted radiation, three cases can be easily evaluated. At a distance very close to the transmitter,

$$\rho = \frac{D_T}{2} \tag{2-10}$$

so

$$\text{diffuse target loss} = \left(\frac{.32\ \lambda\ R}{D_T\ D_R}\right)^2 \tag{2-11}$$

where D_T = transmitter diameter. At one far field distance ($R = d_{FF} = D_T^2/\lambda$) for diffraction limited optics,

$$\rho = D_T \tag{2-12}$$

so

$$\text{diffuse target loss} = \left(\frac{.16\ \lambda\ R}{D_T\ D_R}\right)^2 \tag{2-13}$$

At many far field distances for diffraction limited optics,

$$\rho = \frac{\alpha}{2}\ R \tag{2-14}$$

where α = beam divergence angle. In the diffraction limit,

$$\frac{\alpha}{2} = \frac{1.22\ \lambda}{D_T} \tag{2-15}$$

so,

$$\text{diffuse target loss} = \left(\frac{.16\ D_T}{1.22\ D_R}\right)^2 \tag{2-16}$$

or,

$$\text{diffuse target loss} = 0.017 \left(\frac{D_T}{D_R}\right)^2 \tag{2-17}$$

This last result will be shown in the sections that follow to be incorrect. This error results from the conservative nature of the assumptions made in this section. The assumptions, however, become more valid at distances closer to the collector. Errors involved in Equation (2-11) and Equation (2-13) remain to be evaluated.

More generally,

$$= D_T \left[1 + 1.22 \left(\frac{R}{d_{FF}} - 1\right)\right] \tag{2-18}$$

so the diffuse target loss can be evaluated at all ranges. The range limitations of this technique, however, are not completely understood.

2.4 Far Field Diffuse Target Losses

2.4.1 Introduction

Diffuse targets are frequently encountered by the standard microwave radar system in the form of rain, snow, chaff, and various forms of clutter. Many aspects of the radar response from these targets have already been discussed in some detail (Reference 1) and so the problems are by no means new.

For the intended application there are a few important aspects which require additional attention. In particular, we would like to know: (1) How much heterodyne signal (i.e., coherency) do we lose because of the diffuse random nature of the target? and, (2) For a given transmitting antenna what is the optimum size for the receiving antenna?

In what follows we present a calculation based on a simple yet realistic model of the situation. Analytic expressions are obtained for the variation of the heterodyne signal with size of the receiving antenna and for the amount of coherency lost due to the diffuseness of the target. The results have a straightforward physical interpretation which is discussed.

2.4.2 Target Characteristics - Incoherent Scattering

The target of interest consists of a large amount of small scattering centers (dust particles, water droplets, etc.) distributed diffusely throughout the target volume. While there may be only relatively slow macroscopic variations of the density of these scatterers in space and time, on a microscopic scale the individual scattering particles will be randomly distributed in space and subject to rapid small changes in position and velocity with time (i.e., Brownian motion).

At the receiving antenna therefore the returning radiation consists of a large number of small contributions each with a phase which depends to a large extent on the precise position and velocity of the scattering particle at some instant in time. Since these distances and velocities are random (on the local scale) and are fluctuating rapidly with time in a random manner, the overall result is random phases which effectively decouple the effect of one scattering center from all the others such that the time averaged return signal is incoherent [1]. In addition, if the scattering particles were not all precisely identical then the scattering phase shifts would have a further tendency to vary randomly from particle to particle.

Thus, the effects of such a diffuse target can validly be computed by considering a single scattering center, finding the signal generated in the receiver processing as a result of this scatter alone and summing the independent signal powers arising from all the scatters to obtain the total time averaged incoherent signal which will be observed. In this particular case the processing consists of heterodyning the return signal with a known signal from a stable reference oscillator and observing the magnitude of the detector response generated at the difference frequency (i.e., between the reference and the Doppler shifted return). We therefore must add the heterodyne signal powers due to each of the scatters in the target volume computed as if each were totally independent of all the others.

2.4.3 The Model

For simplicity let us suppose that the scatterers are limited to a thin slab in the xy plane of thickness Δz in which

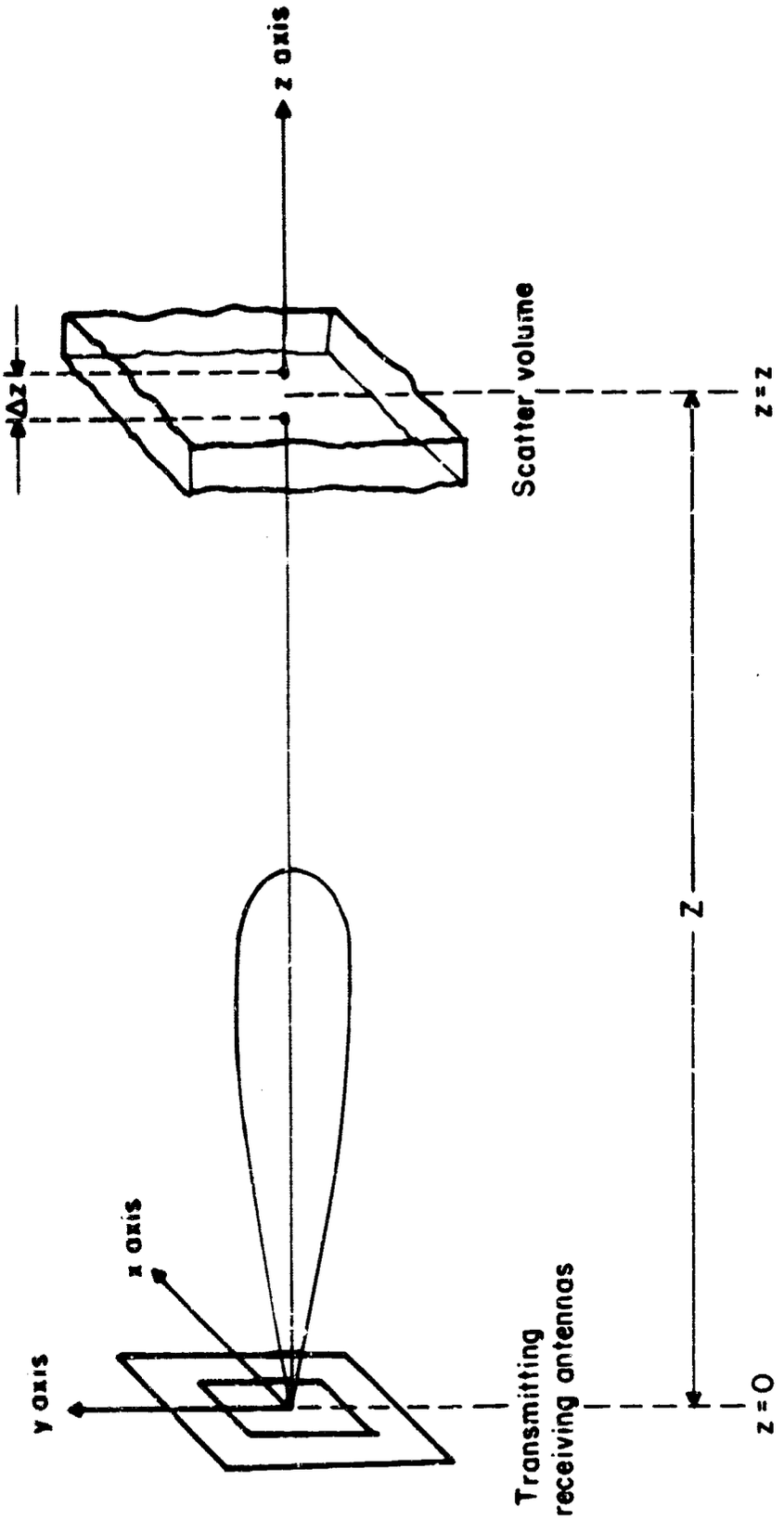
[1] Kerr, D. E., "Propagation of Short Radio Waves", Boston Technical Publishers, Inc., Lexington, Mass. (1964).

they are uniformly and randomly distributed. Without loss of generality we can further assume that all particles have the same average velocity relative to the transmitter-receiver and hence we deal with only a single Doppler shift and only one heterodyne frequency. The general case is easily obtained by summing over all velocities recognizing that the density of particles in the one velocity case refers only to those scatterers having that particular velocity. The Brownian motion velocity effects will be included only in so far as they contribute to making the return "incoherent" and thus permit the calculational procedure suggested above (i.e., sum independent signal powers) - potential Doppler broadening effects are not included explicitly. All particles are assumed to be identical and hence to produce the same intensity backscatter. The transmitting and receiving antennas are assumed to be placed on the Z axis in the xy plane at a large distance z from the scattering layer ($\frac{\Delta z}{z} << 1$) such that the scatters are in the far field of both antennas. When necessary, for mathematical simplicity, the antennas are taken to be square although in practice standard circular antennas are to be anticipated, (See Figure 2-1).

For a wave amplitude E(xyz) propagating along the z axis with diffraction spreading in the xy directions the appropriate approximate form of Huygen's principle is

$$E(xyz) = \frac{2ik}{z} e^{ikz} \iint dx'dy' \; E(x'y'z=0) \; e^{\frac{ik}{2z}\left[(x - x')^2 + (y - y')^2\right]} \tag{2-19}$$

where $k = 2\pi/\lambda$, E(xyz) is the amplitude distribution in the xy plane at z = z and E(xyz = 0) is the amplitude distribution in the xy plane at z = 0, and z is assumed to be large enough that $z/\lambda >> 1$.



CONFIGURATION USED IN THE CALCULATION OF DIFFUSE TARGET LOSSES.

FIGURE 2-1

In the far field with $z \to \infty$ the quadratic terms in the exponential become negligible and we find

$$E(xyz)_{\text{far field}} \simeq \frac{2ik}{z} e^{ikz} \iint dx'dy' \; E(x'y'0) \; e^{-\frac{ik}{z}(xx' + yy')} \tag{2-20}$$

Thus if on the transmitting antenna's surface we have a plane wave distribution of uniform amplitude E_o, then

$$E(xyz=0) = \begin{cases} E_o, & \text{if } (xy) \text{ is within the antenna aperture} \\ 0, & \text{if } (xy) \text{ is outside the antenna aperture} \end{cases}$$

and the incident field in the scattering region at $z = z$ is given by

$$E_{inc}(xyz) \simeq \frac{2ik}{z} e^{ikz} E_o \iint_{\substack{\text{Antenna} \\ \text{Aperture}}} dx'dy' \; e^{-\frac{ik}{z}(xx' + yy')}$$

$$= \frac{iz}{2k} e^{ikz} E_o \left(\frac{\sin \frac{ka_T x}{2z}}{x} \right) \left(\frac{\sin \frac{ka_T y}{2z}}{y} \right) \tag{2-21}$$

where a_T is the length of the edge of the transmitting antenna.

A single particle at the point $\bar{r} = (xyz)$ would scatter a wave back toward the antennas the amplitude of which would be proportional to an appropriately defined backscatter cross-section and to the incident field $E_{inc}(xyz)$ (Equation 2-21). Since the backscatter cross-section is taken to be the same constant for all particles we will make no explicit reference to it and consider simply that the scatterer acts as a point source at (xyz) with a strength proportional to E(xyz). Equation (2-19) can be used

again to compute how the back scattered wave propagates towards the antennas and we find for the scattered field $E_{scat}(x"y"0)$ in the $z = 0$ plane,

$$E_{scat}(x"y"0) \sim \frac{2ik}{z} e^{ikz} E_{inc}(xyz) e^{-\frac{ik}{z}(xx" + yy")}$$

(2-22)

On the receiving antenna in the $z = 0$ plane we also supply a plane wave reference signal $E_{ref}(xy0) = E_{ref} = \text{constant}$, which propagates precisely along the z axis. The total amplitude received is therefore $E_{scat}\, e^{i\omega_0 t} + E_{ref}\, e^{i\omega_1 t}$ and the heterodyne current i_{Het} at the frequency $(\omega_0 - \omega_1)$ will be given by

$$|i_{Het}| \sim \left| \iint_{\substack{\text{Receiving} \\ \text{Antenna}}} E^*_{ref}\, E_{scat}\, dx"dy" \right|$$

$$\sim \frac{2k}{z} |E_{ref}|\, |E_{inc}(xyz)| \iint e^{-\frac{ik}{z}(xx" + yy")}\, dx"dy"$$

$$\sim \frac{z}{2k} |E_{ref}|\, |E_{inc}(xyz)| \left(\frac{\sin \frac{ka_R x}{2z}}{x} \right) \left(\frac{\sin \frac{ka_R y}{2z}}{y} \right)$$

(2-23)

where a_R is the length of the edge of the receiving antenna.

The heterodyne power P_{Het} due to the scatterer at (xyz) will be proportional to the current squared; i.e.,

$$P_{Het} \sim |i_{Het}|^2$$

(2-24)

As discussed above, the total heterodyne power due to all the scatterers in the target volume is given by summing Equation (2-24)over all scatterers. Assuming a uniform distribution of scatterers in the scattering volume with a density N, we find for the total heterodyne power

$$(P_{Het})_{Total} \sim \left|\frac{z}{2k}\right|^4 |E_{ref}|^2 |E_o|^2 N \Delta z \left[\int_{-\infty}^{\infty} dx \left(\frac{\sin \frac{ka_T x}{2z} \sin \frac{ka_R x}{2z}}{x^2}\right)^2 \int_{-\infty}^{\infty} dy \left(\frac{\sin \frac{ka_T y}{2z} \sin \frac{ka_R y}{2z}}{y^2}\right)^2\right] \tag{2-25}$$

We have substituted from Equation(2-21) and assumed that the variation of z within Δz is negligible (i.e. $\frac{\Delta z}{z} << 1$) so that all z's can be taken to be a suitable average such as, z = the distance to the center of the target slab, and the z integration becomes simply

$$\int_{z - \frac{\Delta z}{2}}^{z + \frac{\Delta z}{2}} dz' \, F(z') \simeq F(z) \, \Delta z$$

The integrals in Equation (2-25)are discontinuous but can be readily evaluated to give

$$\int_{-\infty}^{\infty} dx \left(\frac{\sin B_T x \sin B_R x}{x^2}\right)^2 = \pi B_<^2 \left(B_> - \frac{B_<}{3}\right) \tag{2-26}$$

where $B_<$ is the lesser of B_T and B_R and $B_>$ is the greater. In addition the total transmitted power P_T and the total reference signal power P_R can be related to E_{ref} and E_o as

$$|E_o|^2 = \frac{P_T}{a_T^2} = \frac{P_T}{A_T}$$

and

$$|E_{ref}|^2 = \frac{P_R}{a_R^2} = \frac{P_R}{A_R}$$

(2-27)

where $A_T = a_T^2$ = area of transmitting antenna and $A_R = a_R^2$ = area of receiving antenna.

Combining Equations (2-25, 2-26 and 2-27) we obtain finally

$$(P_{Het})_{Total} \sim \left|\frac{2-k}{z}\right|^2 N \, \sigma z \, P_R \, P_T \begin{cases} A_R - \frac{2}{3}\frac{A_R^{3/2}}{A_T^{1/2}} + \frac{A_R^2}{9A_T} & A_R < A_T \\ A_T - \frac{2}{3}\frac{A_T^{3/2}}{A_R^{1/2}} + \frac{A_T^2}{9A_R} & A_R > A_T \end{cases}$$

(2-28)

This is plotted in Figure (2-2) as a function of the area A_R of the receiving antenna. For very small values of A_R the receiving antenna has a wide beam pattern and thus "sees" the scattering volume as if it were a point source and fully coherent. As A_R increases in size the heterodyne signal grows linearly with A_R and the signal remains essentially fully coherent until the

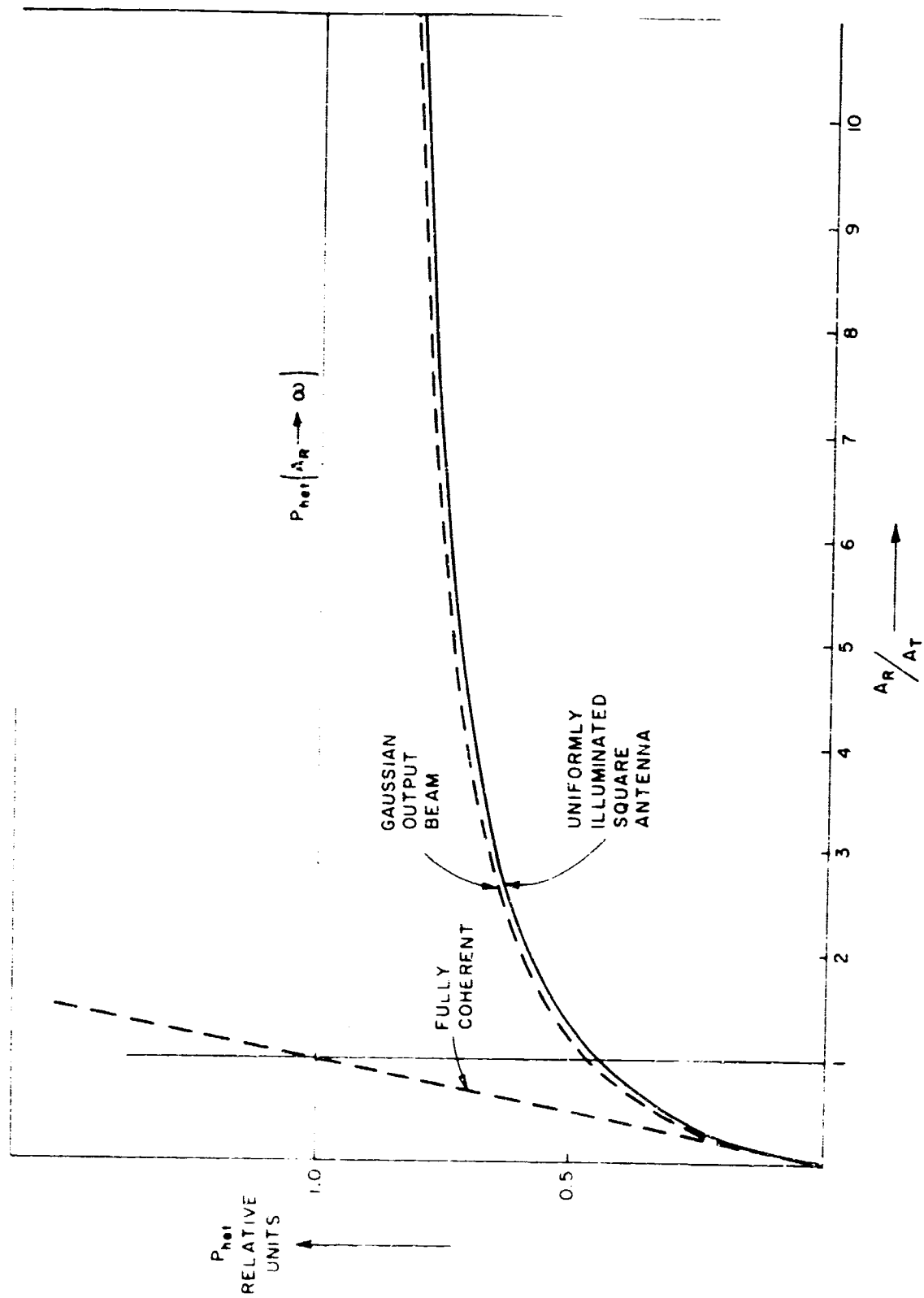


Figure 2-2: Heterodyne Signal from Diffuse Target as a Function of the Receiving Antenna

receiving antenna pattern shrinks enough that the scattering volume no longer appears as a single point source. As the receiving area (A_R) grows significantly larger than the area (A_T) of the transmitting antenna, the region of the scattering volume "seen" by the receiver gets smaller and smaller. Thus the effective backscattered signal source becomes a point source with a strength proportional to $1/A_R$. The total signal collected is proportional to the strength of the effective point source ($1/A_R$) times the area of the receiving antenna (A_R) and hence limits to a constant ($1/A_R \times A_R$) which is independent of the size of the receiving antenna.

In order to calculate the loss in heterodyne signal due to the diffuse nature of the target let us calculate the heterodyne signal which would be obtained if all the backscattered energy received by the antenna was in fact fully coherent. The total energy received by the antenna is given by

$$P_{Total} \sim \underset{\substack{\text{Scattering}\\ \text{Volume}}}{\iiint} N \left|E_{scat}\right|^2 dxdydz \times A_R$$

$$\sim N \Delta z \left|E_o\right|^2 A_R \int_{-\infty}^{\infty} dx \left(\frac{\sin \frac{ka_T x}{2z}}{x}\right)^2 \int_{-\infty}^{\infty} dy \left(\frac{\sin \frac{ka_T y}{2z}}{y}\right)^2$$

$$\sim \left(\frac{\pi k}{2z}\right)^2 N \Delta z P_T A_R \qquad (2\text{-}29)$$

The amplitude of the coherent wave having the same power would be proportional to $\sqrt{(P_{Total})/A_R}$ and the resulting heterodyne current is

$$|i_{Het}| \sim A_R \, |E_{ref}| \sqrt{\frac{P_{Total}}{A_R}} \tag{2-30}$$

and the effective fully coherent heterodyne signal power would be

$$(P_{Het})_{Coherent} \sim |i_{Het}|^2 \sim A_R \, |E_{ref}|^2 \, P_{Total}$$

$$\sim \left|\frac{\pi k}{2z}\right|^2 N \Delta z \, P_R \, P_T \, A_R \tag{2-31}$$

We can now compute the ratio (R) of the actual heterodyne power (Equation 2-28) to the equivalent fully coherent signal (Equation 2-31) to obtain the fractional reduction due to the loss of coherency induced by the diffuse value of the target. We find

$$R = \begin{cases} 1 - \frac{2}{3}\sqrt{\frac{A_R}{A_T}} + \frac{1}{9}\left(\frac{A_R}{A_T}\right) & A_R \leq A_T \\ \frac{A_T}{A_R} - \frac{2}{3}\left(\frac{A_T}{A_R}\right)^{3/2} + \frac{1}{9}\left(\frac{A_T}{A_R}\right)^2 & A_R > A_T \end{cases} \tag{2-32}$$

For small values of A_R we see $R \to 1$ as expected, while for large

values of A_R we find $R \to A_T/A_R \to 0$. This result, expressed in terms of db loss, is presented in Figure (2-3) and represents the answer to the first question.

To answer the second question as to the size of the optimum receiver antenna we see from Figure (2-2) that in fact there appears to be no optimum. An infinitely large antenna gives the maximum signal. However, it is easy to see that one cannot gain a great deal by making the antenna much bigger than the transmitting antenna. The condition of equal antenna size ($A_R = A_T$) results in a signal which is about 45 percent of the maximum possible. Doubling the receiving antenna size (i.e., $A_R = 2A_T$) only improves the signal to 60 percent of the optimum and further gains come slowly.

2.4.4 Gaussian Output

The above calculation can easily be carried out for the case of a Gaussian output beam where the field intensity in the aperture of the transmitting antenna varies as

$$E_o(xyz=0) \sim E_o\, e^{-\frac{x^2 + y^2}{2a_o^2}} \tag{2-33}$$

and there are no important diffraction effects from the edges of the antenna. The receiving antenna, reference signal and scatterers are the same as in the above calculations. Defining an effective transmitter area $A_o = 4\pi a_o^2$ we find for the heterodyne power

$$P_{Het} \sim \left|\frac{2\pi k}{z}\right|^2 N \Delta z\, P_R\, P_T\, A_o \left[\operatorname{erf}\left(\sqrt{\pi}\frac{A_R}{A_o}\right) - \frac{1}{\pi}\sqrt{\frac{A_o}{A_R}}\left(1 - e^{-\pi\frac{A_R}{A_o}}\right)\right]^2 \tag{2-34}$$

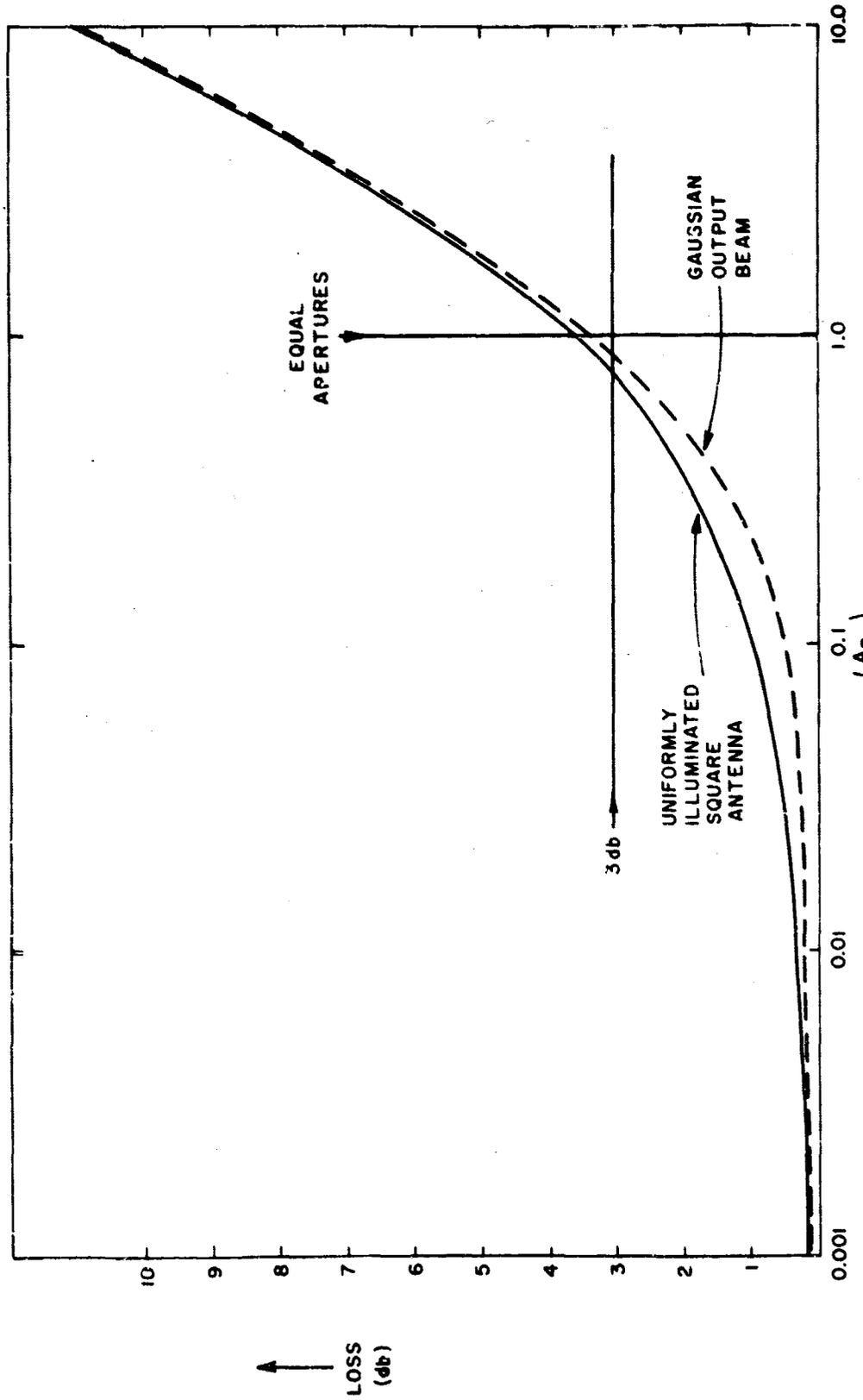


Figure 2-3: Relative Loss of Signal Coherence Due to Diffuse Nature of Target.

where $\mathrm{erf}(x) = 2/\sqrt{\pi} \int_0^x dt\, e^{-t^2}$ = the error function.

For the loss of coherency ($R = P_{Het}/(P_{Het})_{coherent}$) we get

$$R = \frac{A_o}{A_R}\left[\mathrm{erf}\left(\sqrt{\pi \frac{A_R}{A_o}}\right) - \frac{1}{\pi}\sqrt{\frac{A_c}{A_R}}\left(1 - e^{-\pi \frac{A_R}{A_o}}\right)\right]^2 \qquad (2\text{-}35)$$

Again as $A_R \to 0$ we find $R \to 1$ (full coherency) while $A_R \to \infty$, $R \to A_o/A_R$. Thus, by choosing to define the effective transmitter area as $A_o = 4\, a_o^2$, we find the asymptotic loss of coherency is identical to the result obtained for the case of the uniformly illuminated square antenna. Equation (2-35) is plotted in Figure (2-3) along with Equation (2-32). With this interpretation of antenna size we see that in fact with respect to coherency the difference between a uniformly illuminated square antenna of area A_T and a Gaussian output of effective area $A_o = A_T$ is rather small for all values of A_R.

Using the same definition of effective transmitter area, we can plot the heterodyne signal (Equation 2-34) for the Gaussian case on the same graph as the results for the uniformly illuminated case (Figure 2-2) and we see that again there is very little difference between them. What this suggests is that the above simple calculations already contain the essence of the situation and that variations in shape of the antennas (i.e., circular vs square, Gaussian, etc.) will result in only minor changes.

2.5 Comparison of Diffuse Target Analyses

The optical approach to diffuse target loss suffers from its one simplifying assumption. It is unreasonable to approximate the function $2 J_1 (x)/x$ by a step function which equals 1 for $x \leq 1$ and 0 for $x > 1$. So the signal-to-noise ratio of a system using a collector whose diameter is considerably larger than D_{EFF} will be larger than the calculated value.

This problem has been solved for a system operating with a target in the far field of both the transmitter and receiver. In the near field regions, Fresnel integrals appear in the derivation, adding considerable mathematical complexity. A technique to adequately handle the near field - other than the optical method - requires significant development.

3.0 ATMOSPHERIC SCATTERING

3.1 Introduction

In the equations used to determine the signal-to-noise ratio of any system heterodyning from the atmosphere, there is a term, β - the scattering coefficient, that represents the scattering properties of the atmosphere. Previous reports have indicated that scatter from only the aerosol portion (not the molecular components) of the atmosphere are useful. So the value of β used in the signal-to-noise equation should be that portion of the total scattering coefficient due to the aerosols.

This section will discuss the scattering properties of the atmospheric aerosol. First the fundamentals of scattering theory will be briefly discussed. Then the scattering cross-section of spherical particles will be derived. (The particles of an aerosol will be assumed to be spherical, since this will be the case in any time average.) Two theories will be used to evaluate the scattering of individual spherical particles. Rayleigh scattering applies to particles whose radius is less than or equal to the wavelength of the incident radiation divided by 2π. Mie scattering is valid for all spherical particles. However, the difficulties of computation make the Mie formulism relatively unattractive if other methods apply.

To evaluate β, the cross-section of an individual particle must be multiplied by the particle number density. Since the aerosol consists of a distribution of sizes, the product of the scattering cross-section and the particle size distribution must be integrated. The remainder of this section, therefore, analyzes scattering by a collection of particles of different radii, and then discusses models of the size distribution of the particles in the atmosphere. These models have been made on the

basis of experimental data. While this data is not completely reliable, it can be used to give an estimate of β.

3.2 Scattering Theory

A plane monochromatic electromagnetic wave with intensity I_o and wavelength λ is incident on a particle. The scattered light intensity, at a distance R - which is far from the particle - is given by (See Reference 1):

$$I(\theta,\varphi) = \frac{I_o F(\theta,\varphi)}{k^2 R^2} \qquad (3\text{-}1)$$

where k equals $2\pi/\lambda$ and θ is the angle with respect to the propagation direction of the incident wave, and $F(\theta,\varphi)$ can be defined by:

$$F(\theta,\varphi) = \frac{k^2 R^2 I(\theta,\varphi)}{I_o} \qquad (3\text{-}2)$$

Equation (3-2) identifies $F(\theta,\varphi)$ as the relative amount of light intensity scattered in the direction denoted by θ,φ. The scattering cross-section can then be defined as:

$$\sigma_{sc} = \frac{1}{k^2} \int F(\theta,\varphi)\, d\Omega \qquad (3\text{-}3a)$$

or, substituting equation (3-2)

$$\sigma_{sc} = R^2 \int \frac{I(\theta,\varphi)}{I_o}\, d\Omega \qquad (3\text{-}3b)$$

where $d\Omega$ is the element of solid angle, $\sin\theta d\theta d\varphi$. Therefore, in discussing the scattering properties of particles, two concepts are available. The term $F(\theta,\varphi)$ describes the angular variation of the scattered intensity, while the scattering cross-section indicates the total amount of scattered intensity compared to the total amount of incident intensity.

3.3 Rayleigh Scattering Theory

There exists a simplified scattering theory for spherical particles, whose radius is less than or equal to $\lambda/2\pi$, called Rayleigh scattering. (The Rayleigh formulism is excellent for very small particles, but may differ by a factor of two when $r = \lambda/2\pi$.) In this case the electric field of the incident radiation is assumed to induce an electrical dipole moment. These dipoles then become the source of the scattered field which has the pattern of dipole radiation. Let the polarizability tensor have principal value α_1, α_2, and α_3 with eigenvectors $\vec{n_1}$, $\vec{n_2}$, and $\vec{n_3}$. The incident electrical field has components E_1, E_2, and E_3. So the induced dipole is:

$$\vec{p} = \alpha_1 E_1 \vec{n_1} + \alpha_2 E_2 \vec{n_2} + \alpha_3 E_3 \vec{n_3} \tag{3-4}$$

The electrical field of a radiating dipole is given by:

$$|\vec{E}| = \frac{k^2 |\vec{p}| \sin\gamma}{R} e^{-ikR} \tag{3-5}$$

where γ is the angle between $\vec{p}$ and $\vec{R}$. Since (see Reference 2)

$$I = \frac{c}{8\pi} |\vec{E}^2| \tag{3-6}$$

where c = speed of light. Equations (3-5) and (3-6) can be sub-

stituted into Equation (3-3b) to give the Rayleigh scattering cross-section.

$$\sigma_{sc} = \frac{8\pi}{3} k^4 |\alpha|^2 \tag{3-7}$$

where

$$|\alpha|^2 = \ell^2 |\alpha_1|^2 + m^2 |\alpha_2|^2 + n^2 |\alpha_3|^2 \tag{3-8}$$

The letters ℓ, m, n represent the direction cosines of α with respect to the incident electric field. If the polarizability is isotropic,

$$\alpha_1 = \alpha_2 = \alpha_3 = \alpha \tag{3-9}$$

then $\vec{p}$ is in the direction of $\vec{E_o}$, the incident electric field.

The scattered radiation field has two orthogonal plane-polarized components: one with the electric field in the plane of the incident and scattered propagation vectors, and one normal to this plane. For the perpendicular component

$$\gamma = 90^o \tag{3-10}$$

So

$$I_\perp = \frac{k^4 |\alpha|^2 I_o}{R^2} \tag{3-11}$$

For the parallel component

$$\gamma = 90^o - \theta \tag{3-12}$$

$$I_{\parallel} = \frac{k^4 |\alpha|^2 I_o \cos^2 \theta}{R^2} \tag{3-13}$$

and for unpolarized incident radiation

$$I = \frac{k^4 |\alpha|^2 I_o (1 + \cos^2 \theta)}{2R^2} \tag{3-14}$$

In order to determine the scattered radiation pattern of any particle satisfying Rayleigh's criterion of $r \leq \lambda/2\pi$, it is only necessary to know the polarizability of the particle. For spherical particles (see Reference 1)

$$\alpha = \left(\frac{m^2 - 1}{m^2 + 2}\right) r^3 \tag{3-15}$$

where m is the particle's index of refraction at wavelength λ. Therefore, substituting equation (3-15) into Equations (3-7), (3-12) and (3-13) the following relationships are obtained:

$$\sigma_{sc} = \frac{8\pi}{3} k^4 r^6 \left(\frac{m^2 - 1}{m^2 + 2}\right)^2 \tag{3-16}$$

$$I_{\perp} = \frac{k^4 r^6 I_o}{R^2} \left(\frac{m^2 - 1}{m^2 + 2}\right)^2 \tag{3-17}$$

$$I_{\parallel} = \frac{k^4 r^6 I_o \cos^2 \theta}{R^2} \left(\frac{m^2 - 1}{m^2 + 2}\right)^2 \tag{3-18}$$

3.4 Mie Scattering Theory

A more general scattering theory, for spherical particles of any size, has been developed by Mie. (This formulism of course contains Rayleigh scattering in the limiting case of small particles.) Mie solves Maxwell's equation for the three regions of interest: in front of the sphere, within the sphere, and beyond the sphere. Boundary conditions at the surface of the sphere are matched to determine the scattering function. These scattering functions turn out to be a summation of products of Legendre polynomials, Bessel functions, and Neumann functions. Since the advent of high speed computers, many such functions have been evaluated. The details of these solutions will not be discussed here, rather their physical significance will be investigated.

The Mie scattering functions depend upon only two parameters, α - the size parameter, and m - the index of refraction. (The size parameter, α, unfortunately has the same symbol as the polarizability used earlier. The two are not at all related. From now on, the symbol α will refer to the size parameter.)

$$\alpha = \frac{2\pi r}{\lambda} \tag{3-19}$$

Since scattering depends upon α rather than r and λ independently, changes of r and λ by the same multiplicative factor do not alter the scattering pattern. Rayleigh scattering is valid for small values of α. In fact, for $\alpha \leq 1$, Rayleigh scattering is within a factor of two of the Mie result, and the agreement improves as α decreases.

To become more explicit, it is necessary to introduce the concept of scattering efficiency, C. It is defined as (Reference 1)

$$C = \frac{J_{sc}}{\pi r^2} \tag{3-20}$$

and relates the scattering cross-section of a particle to its geometrical cross-section. As an example, the scattering efficiency of Rayleigh scattering for unpolarized radiation is found by substituting Equation (3-16) into Equation (3-20), giving

$$C_{RAY} = \frac{8\,k^4\,r^4}{3}\left(\frac{m^2 - 1}{m^2 + 2}\right)^2 \qquad (3\text{-}21)$$

Substituting Equation (3-19) into Equation (3-21)

$$C_{RAY} = \frac{8}{3}\,\alpha^4\left(\frac{m^2 - 1}{m^2 + 2}\right)^2 \qquad (3\text{-}22)$$

Calculations of C for larger values of α have been made, and a generalized graph of C versus α appears below.

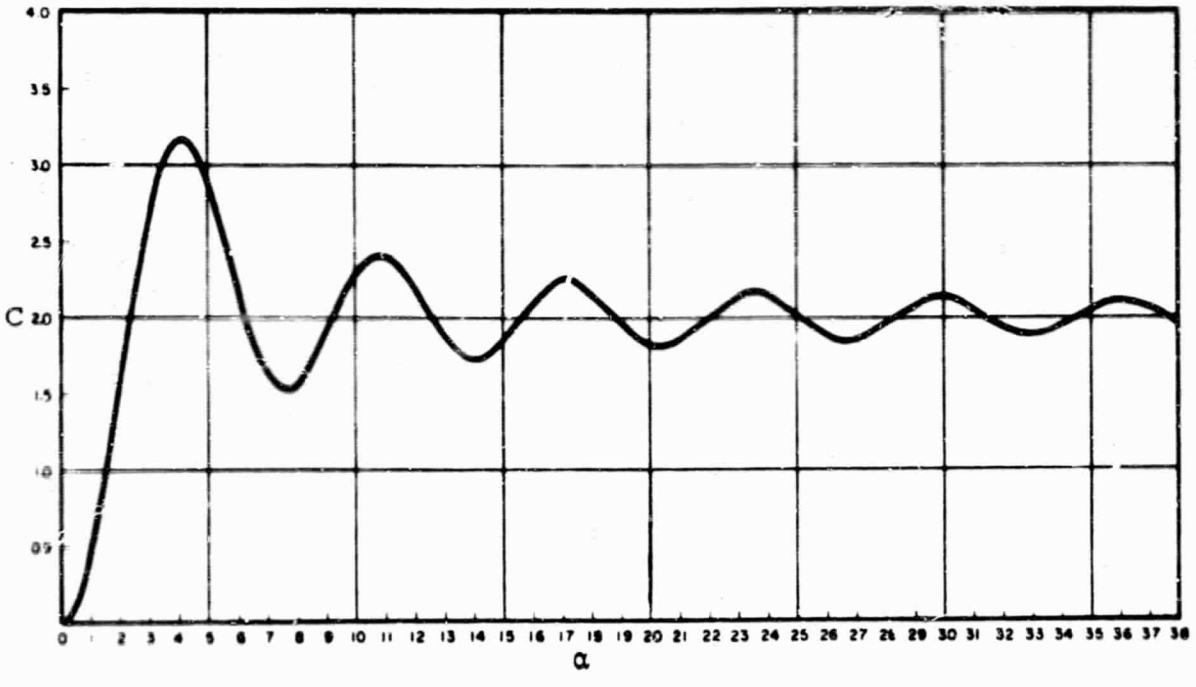


Figure 3-1: Scattering Efficiency versus Size Parameter

The exact form of the curve depends upon m, but several general conclusions can be made. Initially C increases as α^4, then its rate of increase slows up. The initial maximum occurs for a value of α between 5 and 6 and has a value approximately equal to 4. (See Reference 6)

Similar calculations will give the angular dependence of scattering as a function of α and m. The results are similar to those for the total scattering cross-section. However, the oscillations in the angular curves are much greater. The change in the ratio of forward to backscatter as a function of α is of considerable interest. For small values of α, forward and backscatter are equal. As α increases, so does the forward-to-back ratio, which may reach a value of several hundred.

3.5 Aerosol Scattering

The Mie and Rayleigh scattering theories discussed above have evaluated the scattering properties of a single particle. An aerosol consists of a collection of particles (assumed for simplicity to be spherical) of various size and index of refraction. Assume that the atmospheric aerosol can be described by a distribution function $n(r,m)$, where $n(r,m)dr$ is the number of particles with index of refraction m with a radius between r and r + dr. Then

$$\int_0^\infty n(r,m)\, dr = N(m) \qquad (3\text{-}23)$$

where $N(m)$ is the total number of particles with index of refraction m. If $I(\theta,\varphi,r,m)$ is the intensity scattered by a single sphere of radius r and index of refraction m in a direction designated by θ,φ, then the intensity scattered by the entire aerosol is given by:

$$I(\theta,\varphi) = \sum_{m_i} \int_0^\infty n(r,m_i)\ I(\theta,\varphi,r,m_i)\ dr \tag{3-24}$$

To be consistent with Mie theory, r should be replaced by α, giving:

$$I(\theta,\varphi) = \frac{2\pi}{\lambda} \sum_{m_i} \int_0^\infty n(\alpha,m_i)\ I(\theta,\varphi,\alpha,m_i)\ d\alpha \tag{3-25}$$

Since $I(\theta,\varphi,\alpha,m_i)$ can be evaluated by the Mie theory, solution of the aerosol scattering problem is predicated on a knowledge of $n(\alpha,m_i)$.

The term $n(\alpha,m_i)$ is a very difficult, if not impossible, quantity to measure since it involves both the size distribution and the chemical distribution, i.e. index of refraction, of the atmosphere. However, although the scattering for a single particle varies significantly with the particle's index of refraction, the scattering for a collection of particles of various size will depend only slightly upon the refractive indices. (See Reference 3.) This occurs since the different size parameters yield an averaging effect, which will be almost independent of the indices. Therefore, the particle size distribution will be considered, which will be designated as $n(r,h)$ since the distribution changes with altitude, h.

3.6 Particle Size Distribution of Atmospheric Aerosol

There is not much available reliable data on the particle size distribution of the atmospheric aerosol as a function of altitude. The data that does exist shows that the concentrations may vary significantly from day to day. However some useful measurements have been taken from balloons and aircraft. They indicate that

$$n(r,h) = n_o(h)\ r^{-\gamma(h)} \qquad (3\text{-}26)$$

where h is altitude (see References 3,4,5). The term $n_o(h)$ depends strongly on altitude (approximately exponentially). On the other hand, $\gamma(h)$ changes slightly between sea level and 100 km. The measured value of γ differs between experimenters, but all agree that its value lies between three and five for all altitudes.

In order to obtain an estimate of the scattering properties of the atmosphere at 10.6 microns, it is necessary to evaluate Equation (3-25) for the various experimentally obtained values of $n(r,h)$. This will give a range of values for the scattered intensity. The actual value (which will varv with time) should lie within this range.

The need for additional atmospheric aerosol measurements cannot be overly emphasized. For it is only by the techniques discussed here that accurate theoretical estimates of aerosol scattering with 10.6 microns radiation can be made. (Previous numbers used in this program have been obtained by extrapolating the data from Reference 5 to longer wavelengths., Direct measurements of atmospheric scattering should also be made concurrently. The results of these direct experimencs and the theoretical predictions based on particle size distribution

measurements can then be compared. If this comparison is favorable, further theoretical predictions can be trusted in regions where direct measurement is impossible.

REFERENCES

1. van de Hulst, H. C., Light Scattering by Small Particles, John Wiley & Sons, Inc., New York, 1964.

2. Jackson, J. D., Classical Electrodynamics, John Wiley & Sons, Inc., New York, 1962.

3. Bullrich, K., "Scattered Radiation in the Atmosphere and the Natural Aerosol", Advances in Geophysics, Vol. 10, Academic Press, New York, 1964.

4. Curcio, J. A. et al, "Atmospheric Scattering in the Visible and Infrared", NRL Report 5567, 1961.

5. Elterman, L., Atmospheric Attenuation Models, 1964, in the Ultraviolet, Visible, and Infrared Regions for Altitudes to 50 km, AFCRL-64-740, 1964.

6. Penndorf, R., Research on Aerosol Scattering in the Infrared, AFCRL-63-668, 1963.

4.0 EXPERIMENTATION

The objective of the experimental program is to design, fabricate and test an optical heterodyne system for measuring the velocity of air containing a low concentration of particle contaminants. A single mode CO_2 laser operating at 10.6-micron wavelength and a copper-doped germanium detector cooled to liquid helium temperature are the critical components of the present system.

During this program our efforts have been concentrated on measuring Doppler returns from natural and synthetic targets out-of-doors, e.g., clouds, haze, rain, trees, wind-blown smoke, etc., with promising results. Consequently, a low level of effort was applied to the large variety of laboratory measurements which will eventually lead to a calibration of the system and its individual components. In this category, tests were performed on verification of the heterodyne equation, characteristic curves of the detector, noise sources, coherence areas, reflectivity measurements at 10.6 microns, wind tunnel measurements and particle counting.

4.1 Doppler Returns from Leaves, Rain, Haze and Smoke

Doppler returns have been observed from several targets outside the laboratory. The laser beam is directed outside by reflection from an aluminized beam steering mirror positioned over a window and mounted to allow azimuth and elevation positioning. Figure (4-1) shows returns from wind-blown leaves about 500 feet away.

The spectrum of system noise shown on the bottom trace was recorded when the laser beam was blocked between the beamsplitter and the beam steering mirror. The beam was then allowed to propagate to the tree and leaves so that the upper trace could be recorded showing the spectrum of the return Doppler signal plus noise. The signal is the difference between the two traces. At 10.6-micron wavelength, the Doppler frequency is 200 kHz per meter/second of target velocity parallel to the transmitted beam. Since Figure (4-1) has a scale dispersion of 100 kHz/division, the typical leaf velocity component parallel to the laser beam is 0.5 meter/second. The spike near the center of the trace is the zero of Doppler frequency and the zero of target velocity.

Figure (4-2) shows Doppler returns from a moderate rain. The spectrum varied rapidly in time as one would expect since the beam was of small diameter and contained only a few rain drops at any given time. The magnitude of the rain velocity component along the laser beam was between zero and 3 meters/second and the average wind speed just outside the laboratory was 3 meters/second. There was turbulence along the laser beam path.

Strong Doppler signals have been observed from haze on days of high relative humidity as shown in Figures (4-3, 4-4, 4-5, 4-6, 4-7, and 4-8). These returns have peaks around 200 kHz or 1 meter/second velocity component along the beam which had an elevation angle of 20°. The Doppler signals peaked strongly for 5 to 10 seconds and then faded for 20 to 30 seconds. This peaking and fading pattern was typical of the particular prevailing atmospheric conditions. A five-minute sequence of spectra from haze is shown in Figures (4-5 through 4-8). The corresponding system noise can be found in the lower trace of Figure (4-4).

Several outdoor experiments were conducted using smoke as a scattering medium. In one of these tests, smoke was blown into the laser beam by a fan at a distance of fifteen feet. The Doppler return from the turbulent fan-blown smoke is very broad as shown in Figure (4-9) where the zero of Doppler frequency is at the left edge of the screen and the disperions is 500 kHz or 2.5m/sec full scale. The upper curve is the Doppler return and the lower curve is system noise.

The smoke source was turned off and the Doppler return spectra shown in Figure (4-10) was recorded when the smoke had almost entirely dissipated as shown in Figure (4-11). Further spectra of Doppler returns from smoke at a 15-foot range are shown in Figures (4-12) and (4-13). Figure (4-14) shows the smoke generator when Figures (4-12) and (4-13) were made.

Further experiments were carried out using wind-blown smoke at a range of 200 feet as the scattering medium. Figure (4-15) shows the Doppler spectrum with a dispersion of 1 MHz or 5 meters/sec full scale and zero at the left. The appreciable turbulence that existed in the smoke region manifested itself in wide Doppler spectra as shown in Figures (4-15) through (4-18). The Doppler returns peak near 1.5 m/sec with the wind coming at 30° to the laser beam. This corresponds to a wind speed of 1.8 m/sec or about 5 mph which correlates with an anemometer reading between 5 and 10 mph just outside the laboratory.

4.2 Heterodyne Detection Experiments

A set of experiments has been begun in the laboratory that will lead to an optimum utilization of a copper-doped germanium photoconductor in the heterodyne detection mode of operation. Leading toward this goal, preliminary measurements have been made on:

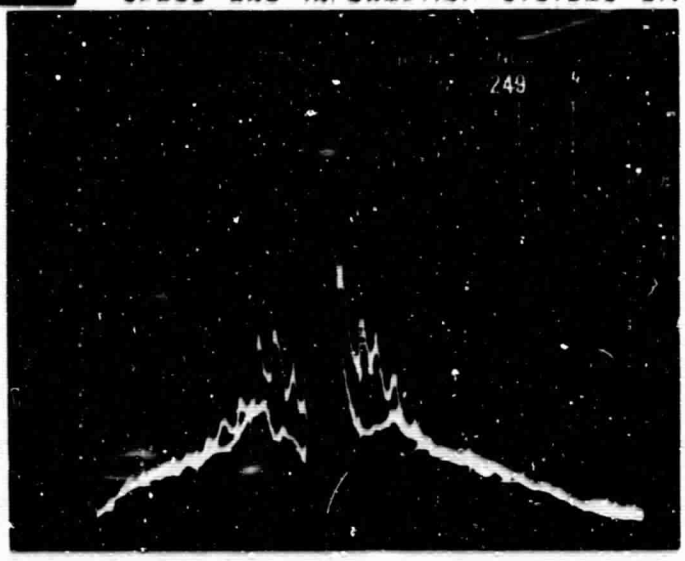


Figure 4-1: Doppler Returns from Wind-Blown Leaves at 500-Foot Range on Top Trace/ System Noise on Bottom Trace - Velocity Dispersion = 0.5 meter/second/division

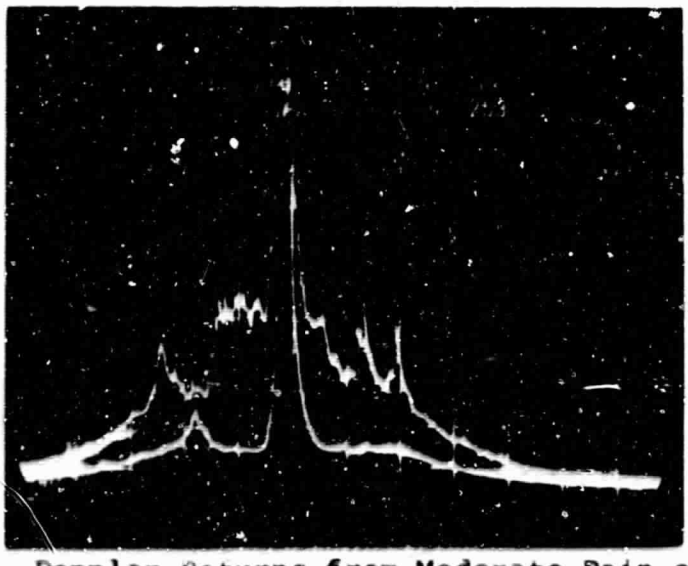


Figure 4-2: Doppler Returns from Moderate Rain on Top Trace/ System Noise on Bottom Trace - Velocity Dispersion Equals 0.5 meter/second/division

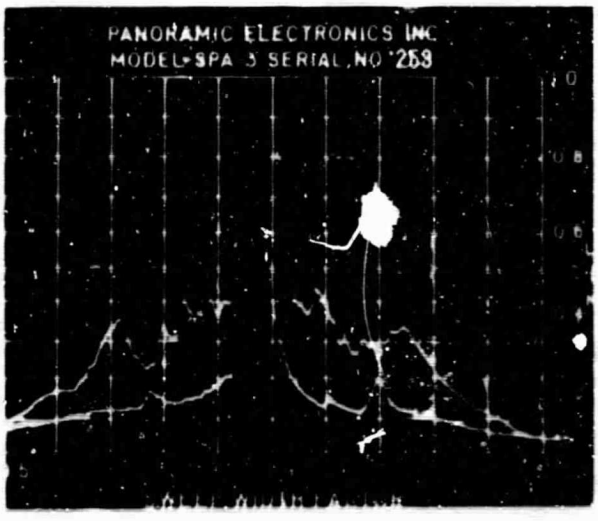


Figure 4-3: Doppler Returns from Haze on a Humid Day on Top Trace/System Noise on Bottom Trace - Velocity Dispersion = 0.5 meter/second/division

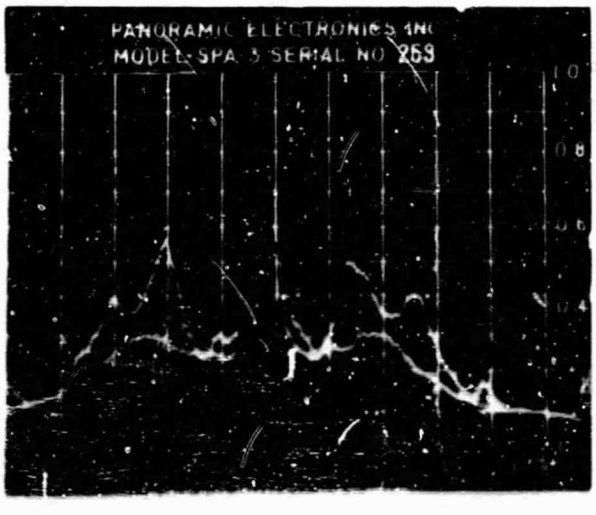


Figure 4-4: Doppler Returns from Haze on a Humid Day on Top Trace/System Noise on Bottom Trace - Velocity Dispersion = 0.5 meter/second/division

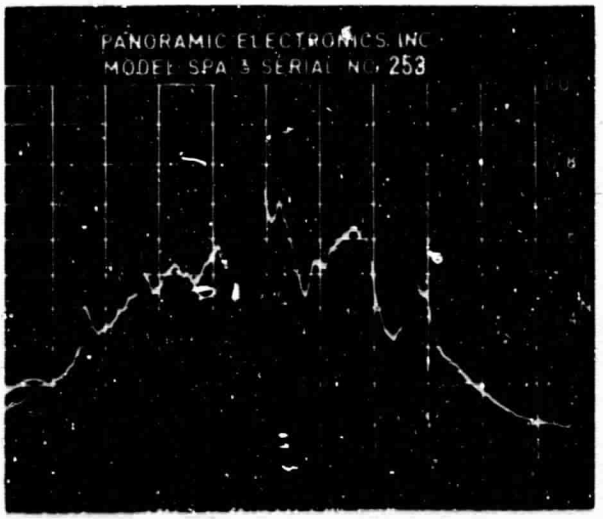


Figure 4-5: Doppler Returns from Haze on a Humid Day - Velocity Dispersion = 0.5 meter/second/division

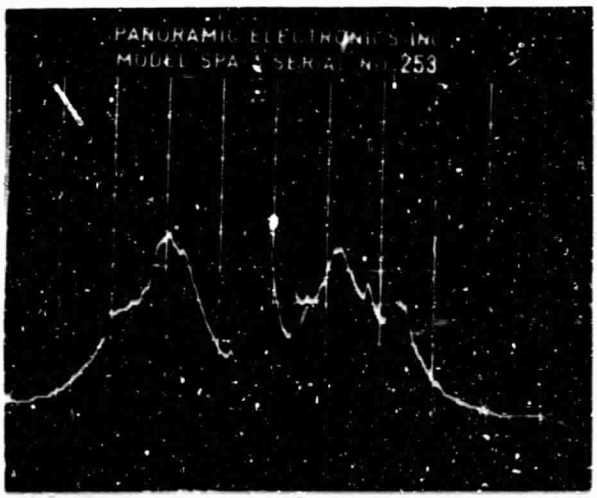


Figure 4-6: Doppler Returns from Haze on a Humid Day - Velocity Dispersion = 0.5 meter/second/division

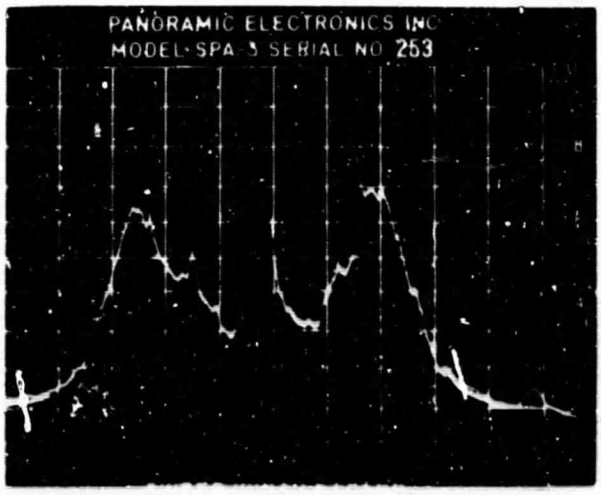


Figure 4-7: Doppler Returns from Haze on a Humid Day - Velocity Dispersion = 0.5 meter/second/division

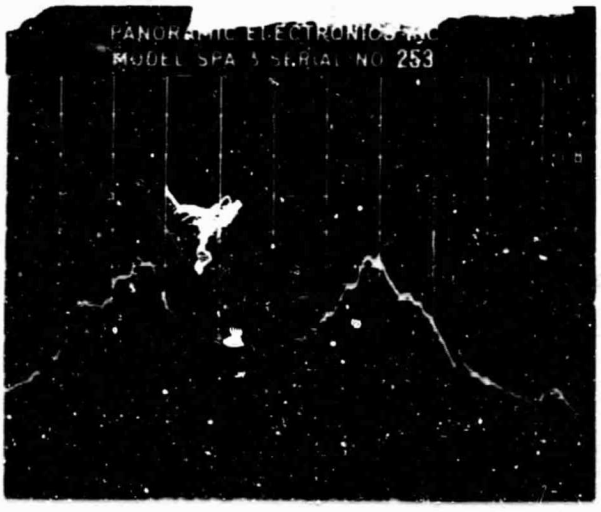


Figure 4-8: Doppler Returns from Haze on a Humid Day - Velocity Dispersion = 0.5 meter/second/division

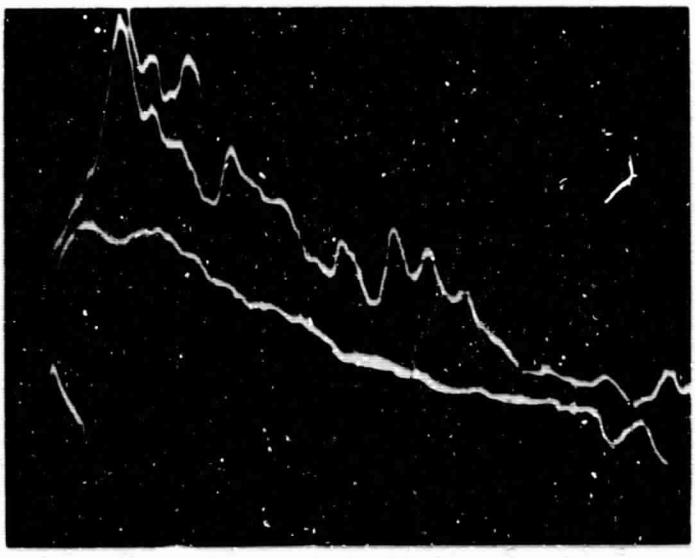


Figure 4-9: Doppler Returns from Wind-Blown Smoke at 15-Foot Range - Velocity Dispersion = 0.25 meter/second/division

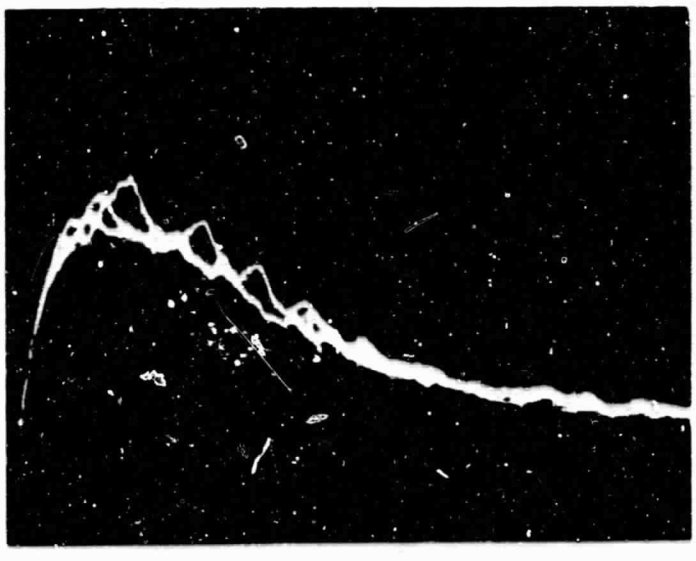


Figure 4-10: Doppler Returns from Smoke which has Dissipated - Velocity Dispersion = 0.25 meter/second/division



Figure 4-11: Smoke Generator Turned Off and Smoke has Mostly Dissipated

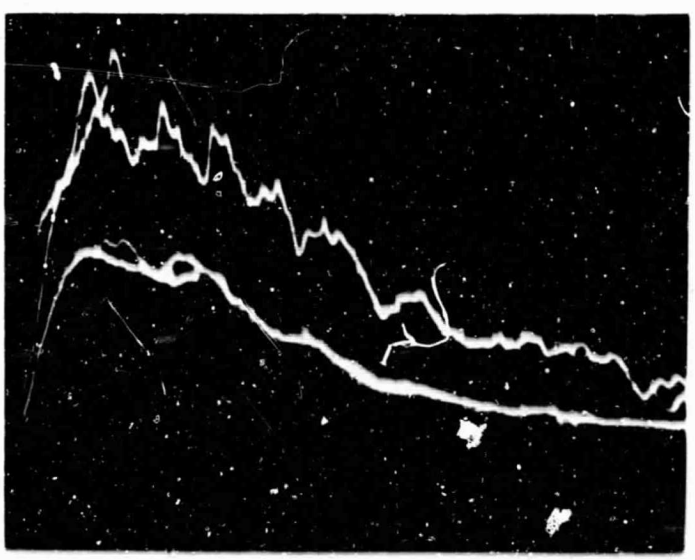


Figure 4-12: Doppler Returns from Smoke at 15-Foot Range - Velocity Dispersion = 0.25 meter/second/division

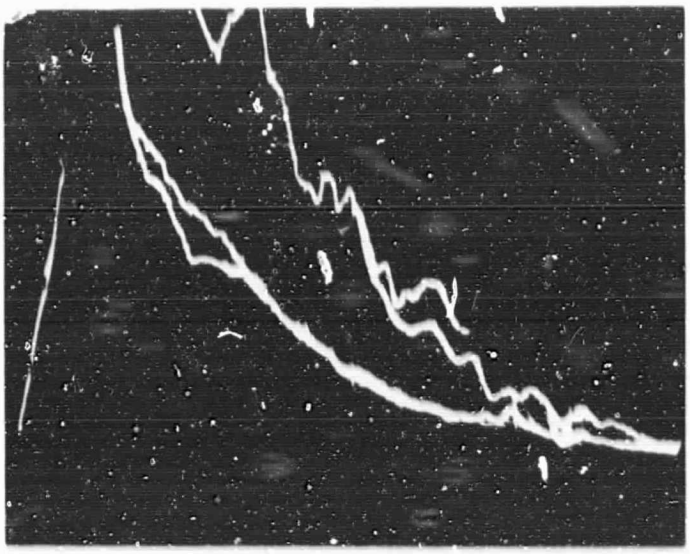


Figure 4-13: Doppler Returns from Smoke at 15-Foot Range - Velocity Dispersion = 0.25 meter/second/division



Figure 4-14: Smoke Generator Setup at 15-Foot Range

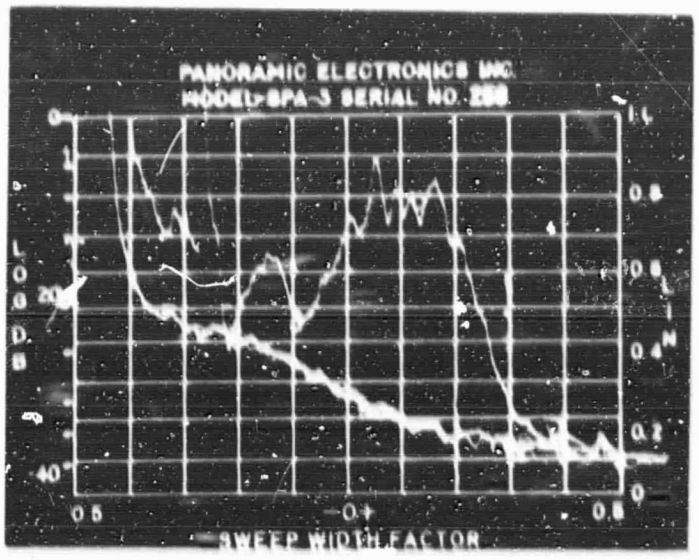


Figure 4-15: Doppler Returns from Wind-Blown Smoke at 200-Foot Range - Velocity Dispersion = 0,5 meter/second/division

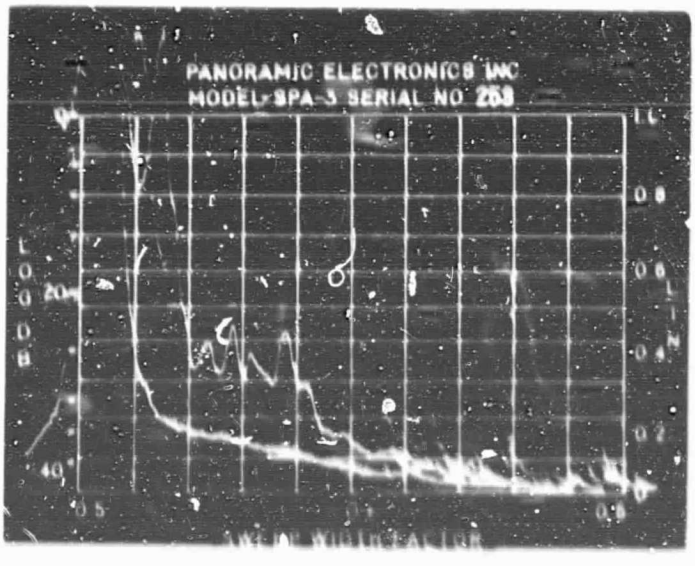


Figure 4-16: Doppler Returns from Wind-Blown Smoke at 200-Foot Range - Velocity Dispersion = 0,5 meter/second division



Figure 4-17: Smoke Generator at 200-Foot Range



Figure 4-18: Smoke Generator at 200-Foot Range

1). Verification of the heterodyne equation.

2). Characteristic curves of the detector.

3). Coherence areas.

4). Noise sources.

Results obtained from these measurements will permit a "figure of merit" to be defined, and will lead to a determination of the operating point that yields a maximum signal-to-noise power ratio for heterodyne detection. These experiments are necessary in order to explain the results of heterodyne signal-to-noise ratio measurements that are 20 db below the level that would be theoretically expected for shot noise limited operation and a quantum efficiency of 50 percent.

4.2.1 Heterodyne Measurements

An attempt was made to verify the heterodyne equation $P_{het} \propto P_{L.O.} P_{sig}$ where P_{het} is the heterodyne power, $P_{L.O.}$ is the local oscillator power at 10.6 microns, and P_{sig} is the signal power that is Doppler shifted from the local oscillator frequency. A Michelson interferometer was set up with a mirror in one arm to give the local oscillator beam and a spinning wheel in the other arm to give the signal beam. The spinning wheel was calibrated with a thermopile as described in Section 4.2.4 of this report so that the signal power could then be calculated from the wheel reflectivity, the geometry, and the incident power at 10.6 microns.

The apparatus was set up and used with a CO_2 laser source and a copper doped germanium detector. $P_{L.O.}$ was measured with a commercially available power meter; P_{sig} was calculated from P_{LO}, the optical parameters of the system, the geometry and the wheel reflectivity; and P_{het} was measured on a spectrum analyzer.

A variety of optical attenuators (beam splitters) was inserted in the arms of the Michelson interferometer in an attempt to verify the heterodyne equation

$$P_{het} \propto P_{L.O.} \, P_{sig} \qquad (4\text{-}1)$$

With $P_{L.O.}$ in the range of 100 mw to 300 mw, where shot noise limited operation is expected, it was shown that the heterodyne equation does not apply as written above. For instance, when P_{sig} was decreased by a factor of 4, P_{het} decreased by a factor less than 4. In these experiments the coherence area was unaltered by insertion of the optical attenuators.

4.2.2 Characteristic Curves

The characteristic curves of the detector were measured with a CO_2 laser as a source. The measurements were coherent in the sense that the laser emits a beam which is coherent in both space and time. However, heterodyning was not involved in the measurements which are shown in Figures 4-19 through 4-24.

The operating point can be specified by the bias voltage V, the bias current I, and the incident infrared power P. The voltage can be written as a function of the current and power

$$V = V(I,P) \qquad (4\text{-}2)$$

For small changes in current and power, there is a corresponding small change in the voltage given by

$$\Delta V = \left(\frac{\partial V}{\partial I}\right)_P \Delta I + \left(\frac{\partial V}{\partial P}\right)_I \Delta P \qquad (4\text{-}3)$$

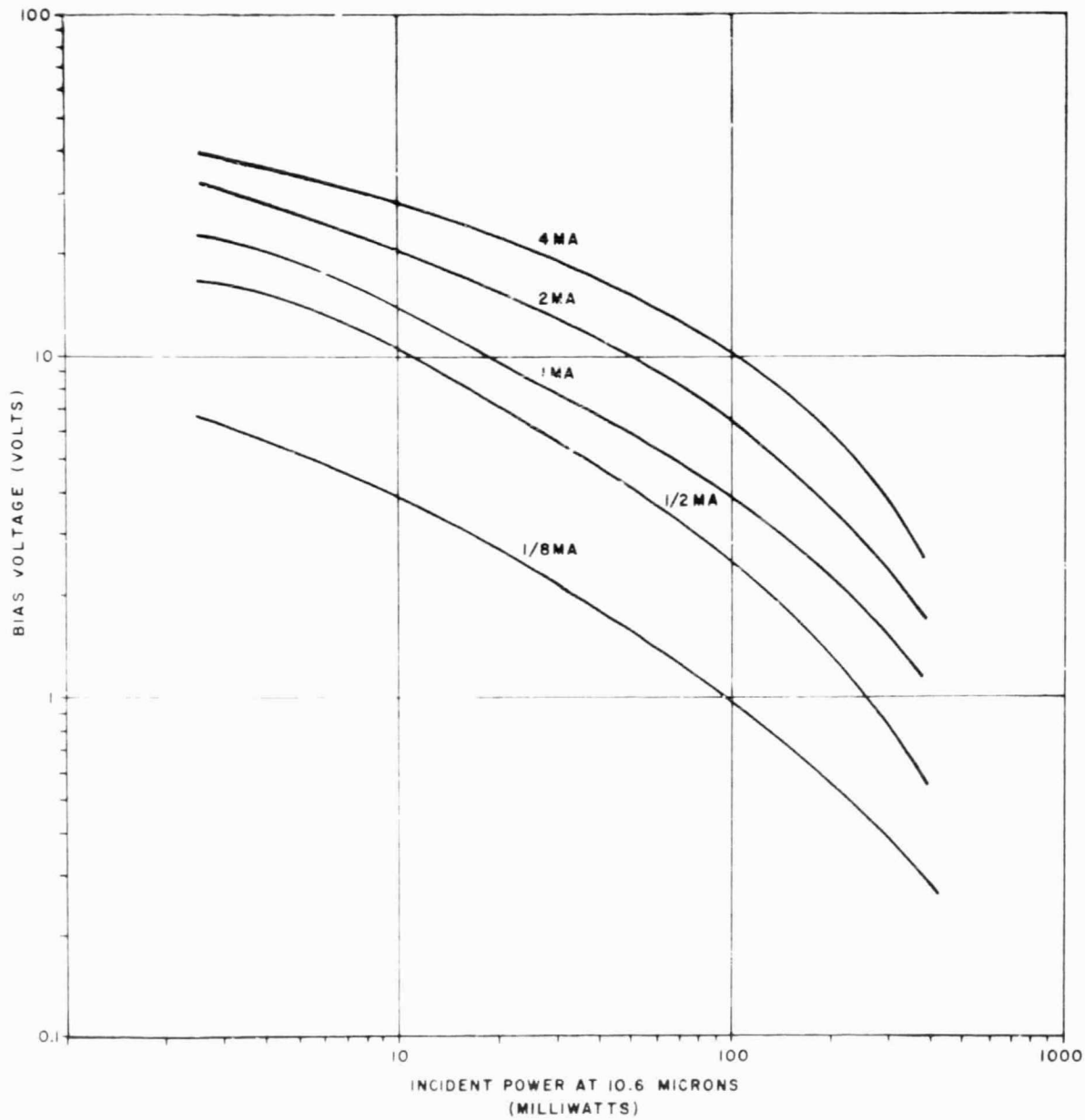


Figure 4-19: Bias Voltage vs Incident Power at 10.6 Microns for Constant Bias Current

Raytheon QKN-1207-144 Cu:Ge Detector

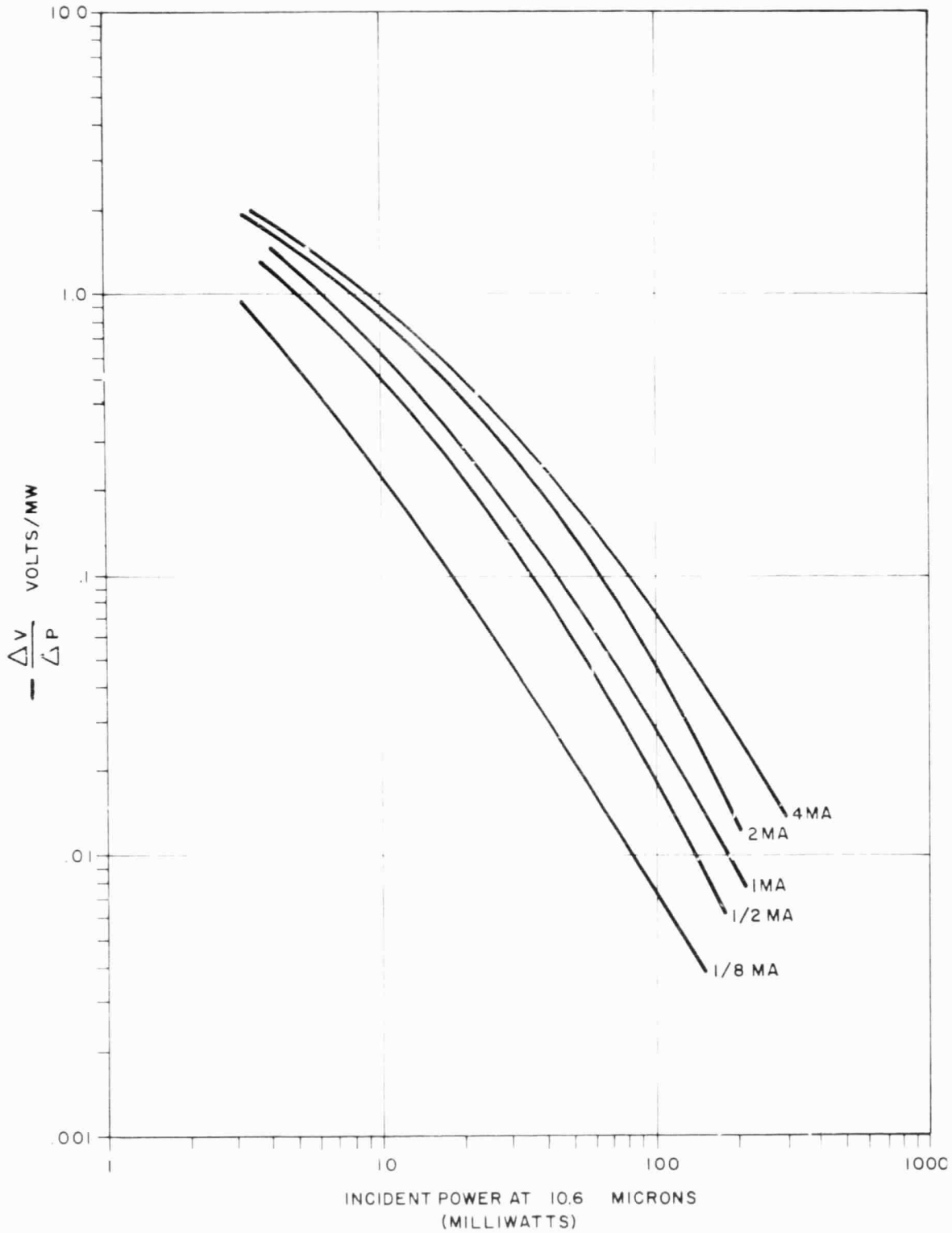


Figure 4-20: $\Delta v/\Delta p$ at Constant Bias Current vs Incident Power at 10.6 Microns

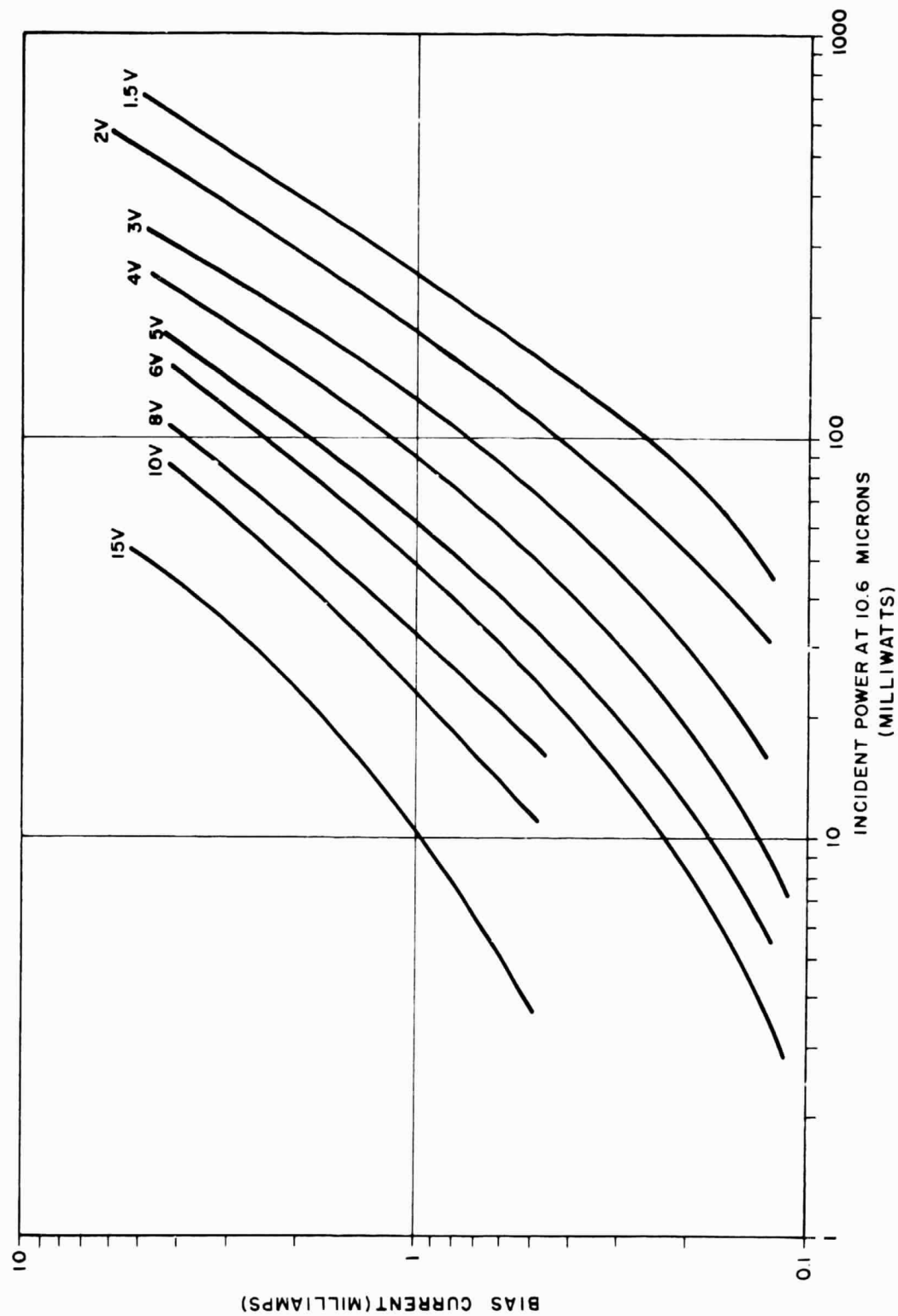


Figure 4-21: Bias Current vs Incident Power for Constant Bias Voltage

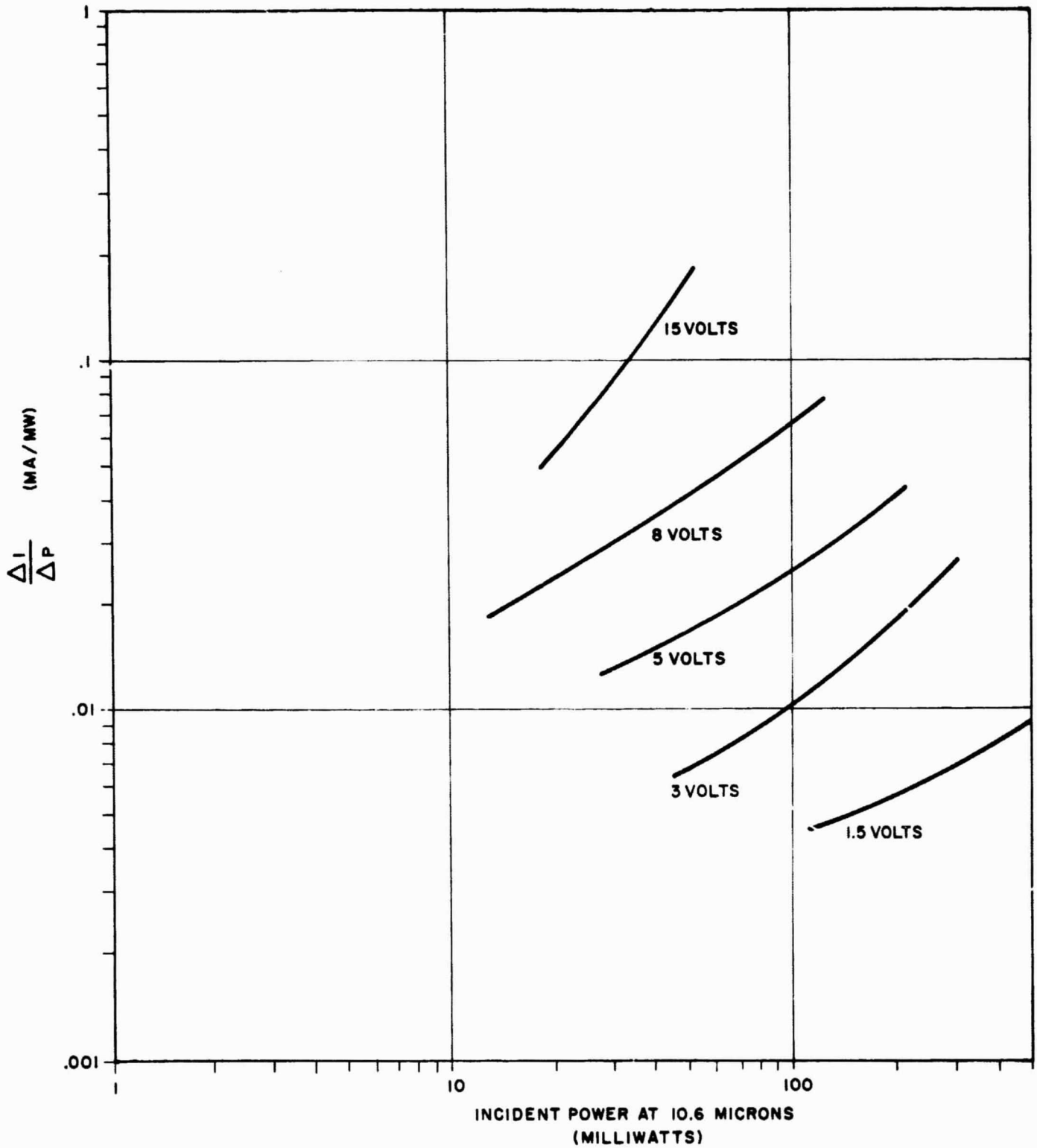


Figure 4-22: $\Delta I/\Delta P$ at Constant Bias Voltage vs Incident Power

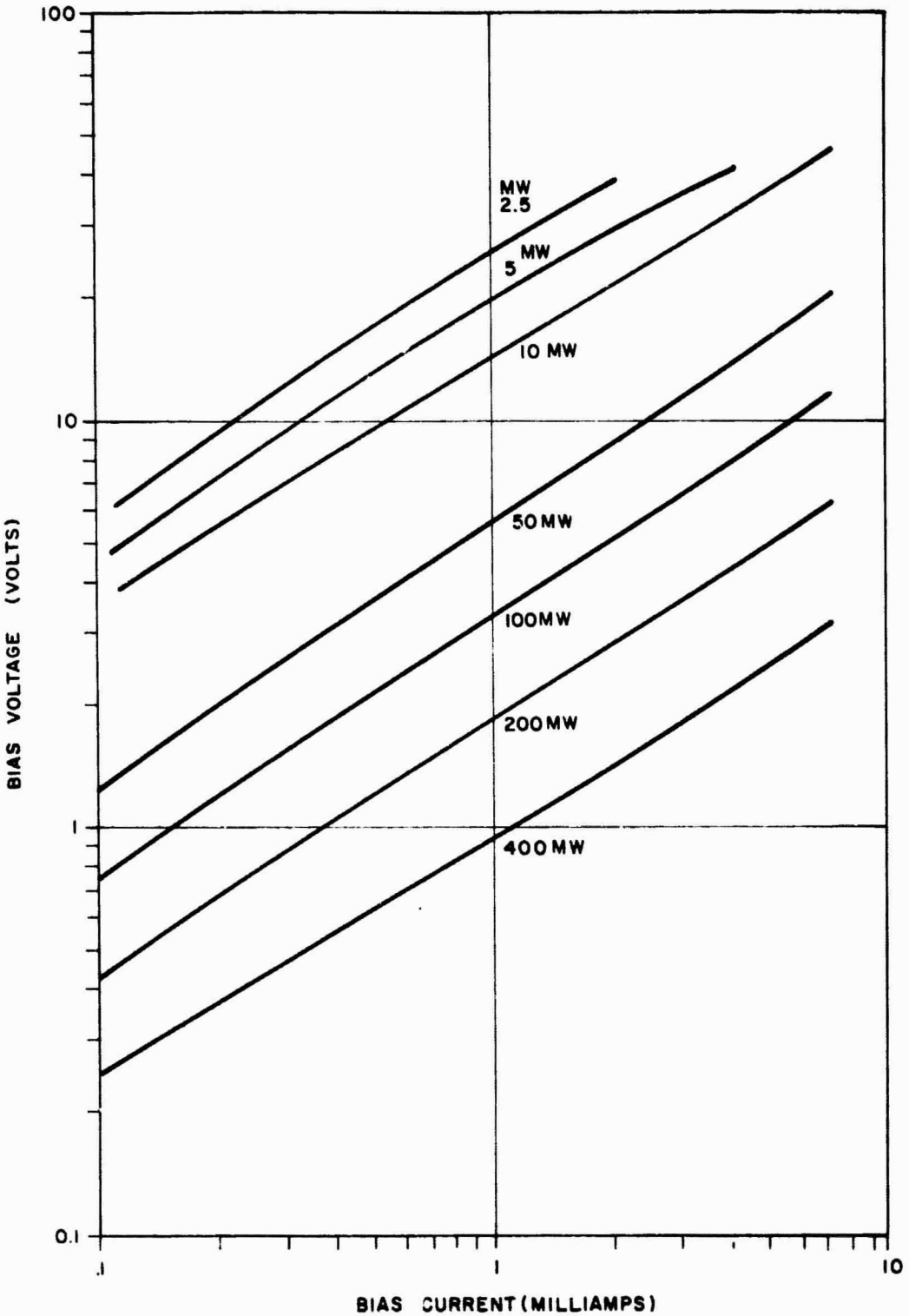


Figure 4-23: Bias Voltage vs Bias Current for Constant Incident Power

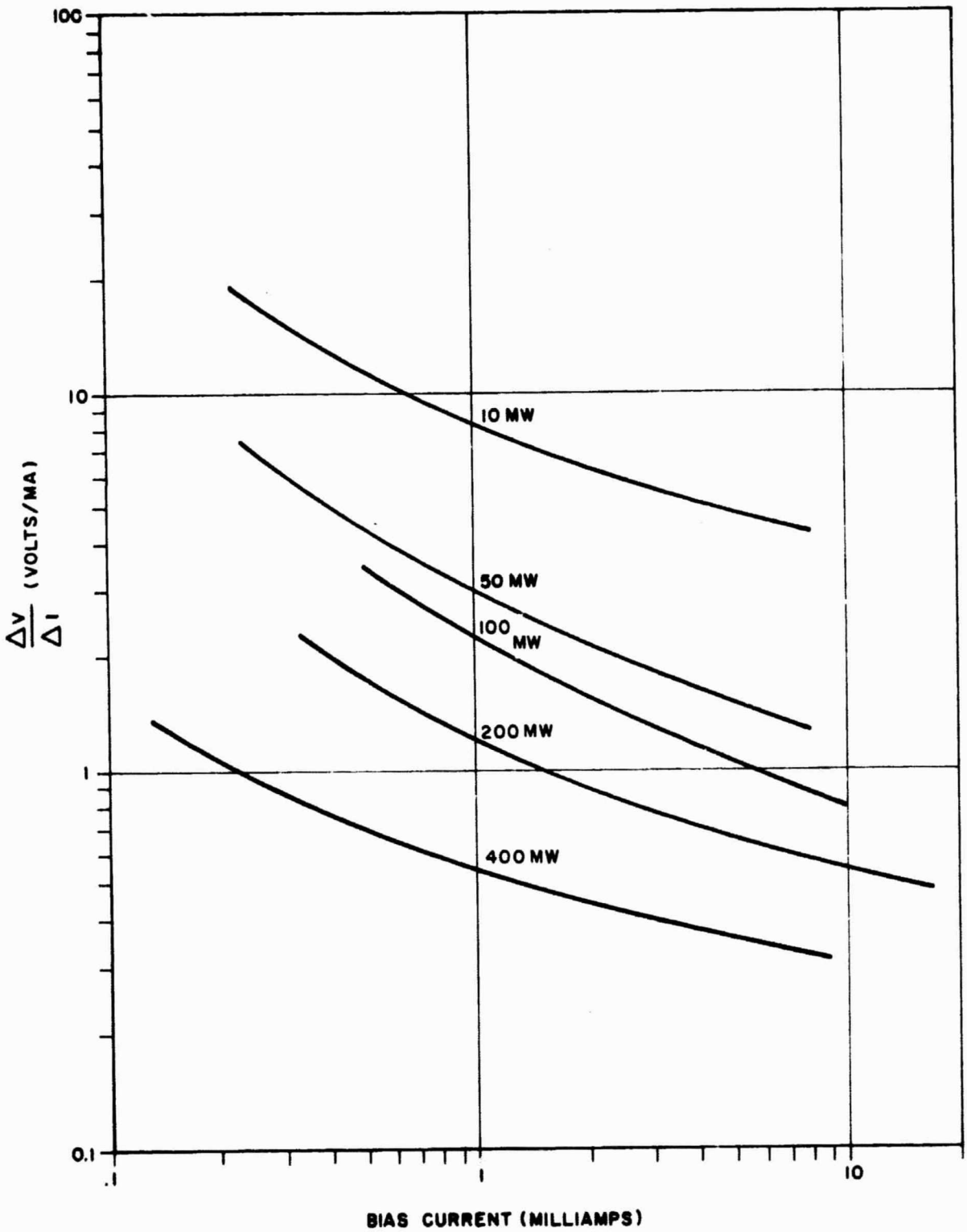


Figure 4-24: Δv/ΔI at Constant Incident Power vs Bias Current

Similarly, we may write

$$I = I(V,P) \tag{4-4}$$

$$\Delta I = \left(\frac{\partial I}{\partial V}\right)_P \Delta V + \left(\frac{\partial I}{\partial P}\right)_V \Delta P \tag{4-5}$$

The partial derivative can be written as

$$\left(\frac{\partial V}{\partial I}\right)_P = \frac{1}{\left(\frac{\partial I}{\partial V}\right)_P} = Z_{A.C.} \tag{4-6}$$

$$\left(\frac{\partial V}{\partial P}\right)_I = \rho_V \tag{4-7}$$

$$\left(\frac{\partial I}{\partial P}\right)_V = \rho_I \tag{4-8}$$

Where $Z_{A.C.}$ is the A.C. impedance, ρ_V is the voltage responsivity and ρ_I is the current responsivity. Thus we have

$$\Delta V = Z_{A.C.}\Delta I + \rho_V \Delta P \tag{4-9}$$

$$\Delta I = \frac{1}{Z_{A.C.}} \Delta V + \rho_I \Delta P \tag{4-10}$$

The values of $Z_{A.C.}$, ρ_V and ρ_I can be determined for any operating point by using the characteristic curves of Figs. 4-19 through 4-24.

With the information discussed above, a heterodyne power function can be derived which gives the heterodyne power as a function of the local oscillator power, the signal power, the bias voltage and/or the bias current. In other words, the operation of the detector in the heterodyne mode is dependent upon the bias conditions as shown by the characteristic curves and the appropriate functions of these curves.

In addition to the measurements discussed above, preliminary noise measurements have been made as a function of bias current. These measurements, discussed in Section 4.2.5, when analyzed in conjunction with those above, will allow a determination of signal-to-noise power ratio for heterodyne detection as a function of the operating point. The operating point corresponding to maximum signal-to-noise can then be found.

4.2.3 Coherence Areas

Some preliminary coherence area experiments indicate that the range dependence that was theoretically predicted earlier is essentially correct; i.e., there is no range dependence in the near field and there is an inverse range squared dependence in the far field. The experimental system used for these measurements consisted of a Michelson interferometer with a mirror in one leg to give a local oscillator beam and a spinning wheel in the other leg to give a Doppler shifted signal beam. The spinning wheel was moved away from the beam splitter and the Doppler signal was observed on a spectrum analyzer. A constant local oscillator beam was used throughout these experiments.

The angle of the wheel with respect to the incident beam and the wheel speed were also held constant. The total signal power $P_{S.T.}$ received on the copper doped germanium detector goes as the reciprocal of the square of the range, or

$$P_{S.T.} \propto \frac{1}{R^2} \qquad (4\text{-}11)$$

and the coherence diameter D_{coh} is proportional to λ/α where λ is the wavelength and α is the angular radius of the illuminated region on the spinning wheel.

$$D_{coh} \propto \frac{\lambda}{\alpha} \tag{4-12}$$

For small angles α can be written as

$$\alpha = \frac{r}{R} \tag{4-13}$$

where r is the radius of the illiminated spot. Hence,

$$D_{coh} \propto \frac{\lambda R}{r} \tag{4-14}$$

The coherent signal power $P_{.coh}$ is proportional to the product of $P_{S.T.}$ and the coherence area which in turn is proportional to the square of the coherence diameter.

$$P_{S.coh} \propto P_{S.T.} D^2_{coh} \tag{4-15}$$

$$P_{S.coh} \propto \left(\frac{1}{R^2}\right)\left(\frac{\lambda R}{r}\right)^2 \tag{4-16}$$

$$P_{S.coh} \propto \frac{\lambda^2}{r^2} \tag{4-17}$$

The wavelength λ is constant, so that

$$P_{S.coh} \propto \frac{1}{r^2} \tag{4-18}$$

For a constant local oscillator power, the heterodyne power P_{het} is directly proportional to the coherent signal power, so that

$$P_{het} \propto \frac{1}{r^2} \tag{4-19}$$

In the near field which corresponds to ranges significantly less than D^2/λ where D is the transmitter aperture diameter $\left(\frac{D^2}{\lambda} = 15 \text{ ft for the setup}\right)$, the radius r is constant and P_{het}

should be independent of range. This was experimentally verified by noting that the spectrum analyzer display of P_{het} was constant for any location of the spinning wheel within the near field region discussed above. In the transition region a range dependence began to develop, and from ranges of 15 ft $<$ R $<$ 30 ft, the dependence $P_{het} \quad \frac{1}{R^2}$ was obeyed. Measurements were terminated at a range of 30 feet due to limited laboratory space.

4.2.4 Wheel Reflectivity Measurements

An experiment was established to measure the absolute reflectivity of several solid materials; see Figure (4-25). These materials were mounted on a wheel which was positioned so that it could be rotated about a vertical axis, which maintained a constant distance between the illuminated spot on the wheel and the detector regardless of wheel angle.

A 40-40 beamsplitter was located to separate the incident and reflected beams. The reflected beam was measured with a calibrated Eppley thermopile while the laser power was monitored by a CRL power meter. The angle between the incident beam and the perpendicular to the wheel face was varied from -50° to $+50^{\circ}$.

Various grades of emery paper, black velvet and magnesium oxide were used as targets on the spinning wheel. These results allow a rapid and accurate determination of the scattered signal power which is required to make heterodyne calibration measurements as discussed in Section 4.2.1.

Data taken from a felt wheel is shown in Table 4-1 with the results of subsequent analysis. Columns I, II and III represent the angle of scattering, the output of the calibrated Eppley thermopile, and the instantaneous laser power respectively. Since the Eppley gave a background reading of 36 μV, the fourth column equals the second column minus 36 μV. Column V represents the normalized results, i.e. the Eppley output which would have been obtained if the incident power equalled 5.1 watts. The Eppley

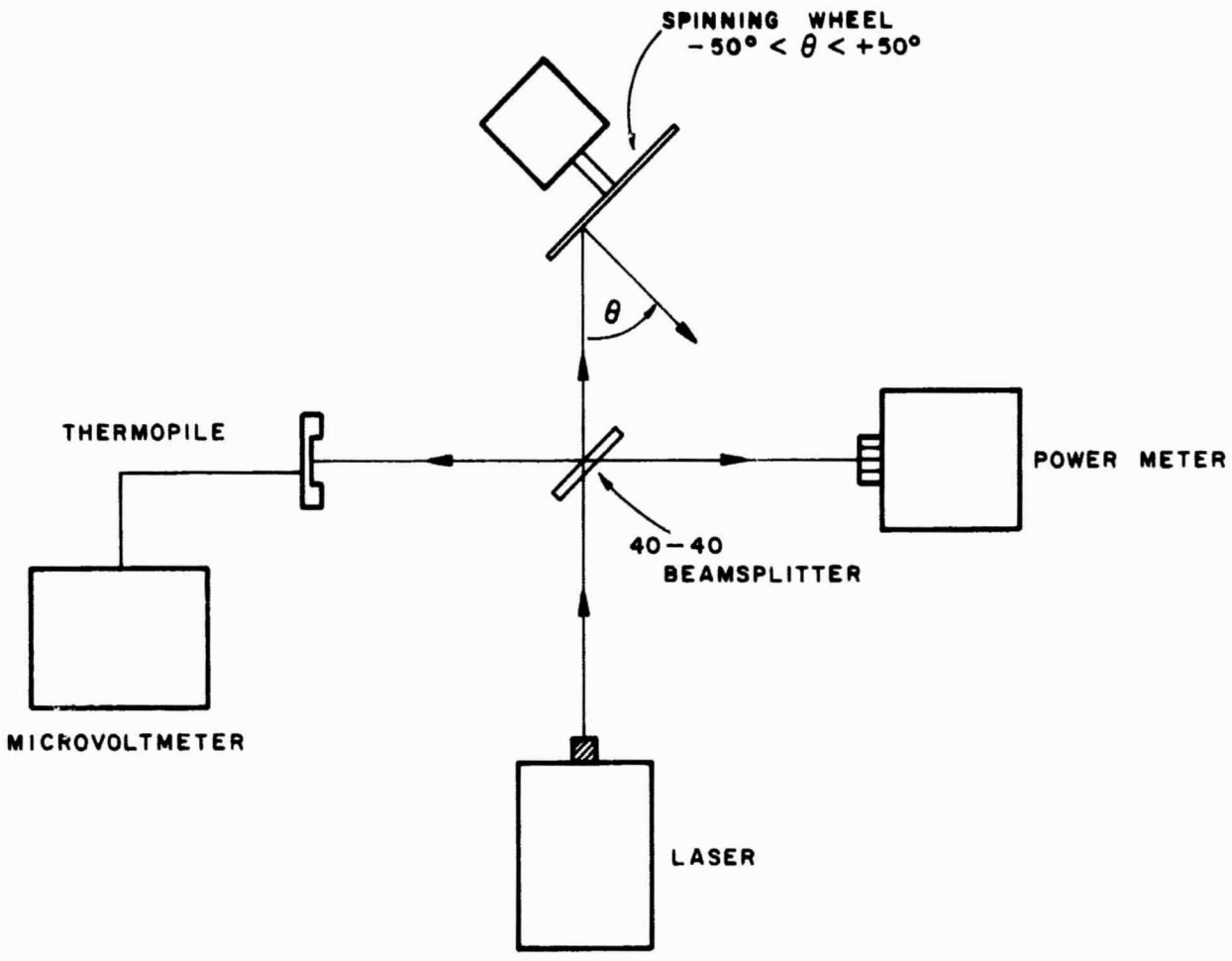


Figure 4-25: Experimental Setup for Wheel Reflectivity Measurements

was calibrated at 0.113 μV/μW and therefore Column VI represents the actual scattered power detected. Finally, the scattered return from a Lambertian reflector referenced to the same output at 0^{o} is given in Column VII.

TABLE 4-1

REFLECTIVITY DATA FROM FELT WHEEL

I	II	III	IV	V	VI	VII
	Epp (μV)	P_{LA} (W)	Epp-B (μV)	$(Epp-B)_N$ (μV)	P_{Sc} (μW)	P_{LAM} (μW)
50	63	5.1	27	27	240	260
40	70	5.1	34	34	300	310
30	72	5.1	36	36	320	350
20	76	5.1	40	40	350	390
10	80	5.1	44	44	390	400
0	83	5.2	47	46	410	410
-10	80	5.3	44	42	370	400
-20	76	5.3	40	38	340	390
-30	71	5.3	35	34	300	350
-40	69	5.3	33	32	280	310

The data on backward scatter from Table (4-1) was used to check the system performance. From this data the reflectivity in the backward direction can be obtained. The system used to make the measurements is illustrated in Figure 4-26 where a spinning wheel replaces the wind tunnel. The beam splitter has a transmissivity (t) and a reflectivity (r). As the laser transmits a power P_o, the measured power is

$$P_{LA} = r\, P_o \qquad (4\text{-}20)$$

and the incident power on the wheel is

$$P_{INC} = t\ P_o \tag{4-21}$$

The reflected power for a target with reflectivity ρ

$$P_{REF} = \rho\ t\ P_o \tag{4-22}$$

while the power reflected by the beamsplitter toward the detector is

$$P_{DET} = r\ \rho\ t\ P_o \tag{4-23}$$

Finally the measured power is given by

$$P_{sc} = \frac{r\ \rho\ t\ P_o\ \pi\ D_{EP}^2}{4R^2} \tag{4-24}$$

where: D_{EP} = diameter of the Eppley thermopile
R = distance from Eppley to target

Substituting Equation (4-20) into Equation (4-24) and re-arranging terms:

$$\rho = \frac{4R^2\ P_{sc}}{t\ P_{LA}\ \pi\ D_{EP}^2} \tag{4-25}$$

Using numbers from Table 4-1 for 0^o and

D_{EP} = 9.53 mm
R = 283 mm
t = 0.4

then the wheel reflectivity in the backward direction, $\rho(o)$, may be calculated to be

$$\rho(o) = 0.226$$

If a heterodyne detector were placed at the location of the Eppley, the expected signal-to-noise ratio should be

$$\frac{S}{N} = \frac{\eta P_s}{2 h \nu B} \tag{4-26}$$

Since,

$$\eta = 0.5 \tag{4-27}$$

$$P_s = 410\ \mu W \left(\frac{2}{9.53}\right)^2 = 18.1\ \mu W \tag{4-28}$$

because the copper-doped germanium detector has an aperture of 2 mm, while the Eppley has a 9.53 mm aperture. The specturm analyzer has a bandwidth of 7 kHz, so

$$\frac{S}{N} = 3.45 \times 10^{10} \tag{4-29}$$

$$\frac{S}{N} \simeq 105\ db \tag{4-30}$$

The results of this experiment indicated that the measured signal-to-noise ratio was approximately 80 db. Because of the discrepancy of 25 db between the theoretical calculation and actual measurements, a detailed experimental analysis of the Cu:Ge detector was initiated.

4.2.5 Noise Measurements

There are several noise sources involved in the heterodyne detection system using a Cu:Ge detector, a low noise preamplifier and spectrum analyzer. Experiments were carried out to determine the noise voltage generated by each noise source.

First, the noise produced by the spectrum analyzer was found to be negligible. Next, the preamplifier was checked for noise output for several different input impedances. This noise voltage was found to be quite low but not completely negligible.

An experiment was set up to measure the noise spectrum for various bias currents with constant local oscillator (LO) power on the copper-doped germanium detector. The LO was then changed

to a new level and the measurements were repeated, using the circuit shown in Figure (4-26). Figure (4-27) shows the detector noise spectrum with bias currents ranging from 3.7 to 0.6 ma. No LO was used. The noise decreased as the bias decreased. When an LO of 11.5 mw was used, the noise spectrum dropped and the effect of the bias noise became smaller. Figure (4-28) shows the noise spectrum for an LO power of 11.5 mw. In Figures (4-27) and (4-28) the spurious signals near the right edge of the screen are generated by a local radio station.

4.2.6 Wind Tunnel Experiments

One objective of this work was to measure atmospheric wind velocity and local wind turbulence by methods of optical heterodyning with a CO_2 laser.

The "clean" air or atmospheric wind contains small contaminate particles by which some of the laser energy is scattered. The detection of this scattered energy is prerequisite to obtaining optical heterodyning.

In order to obtain quantitative data on the important parameters of the detection system, it was desirable to obtain a small wind tunnel to simulate certain atmospheric conditions and to provide a standard source for the calibration of the system.

In particular, the wind tunnel must accept a varying concentration of contaminate particles, to simulate an almost "clean" air, to a "dirty" air with much contamination where signal-to-noise ratios of the detection system are very high for calibration purposes.

The wind tunnel must also be relatively free of turbulence so that read out bandwidth broadening due to turbulence may be distinguished from the bandwidth broadening due to optical and instrument broadening.

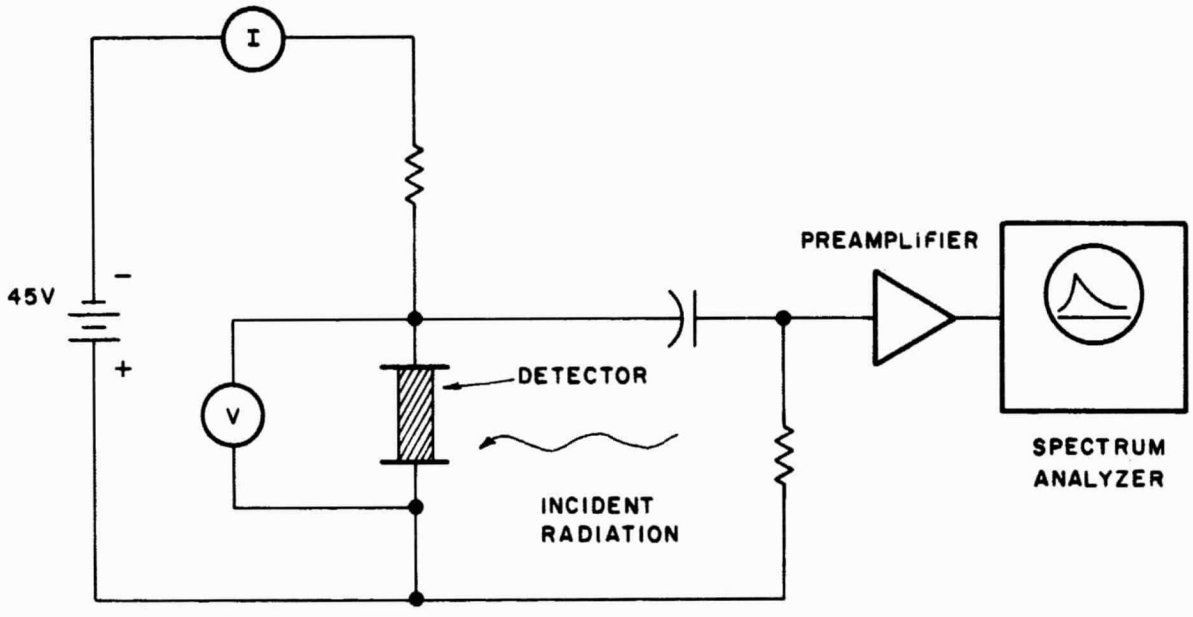


Figure 4-26: Circuit for Detector Noise Measurements

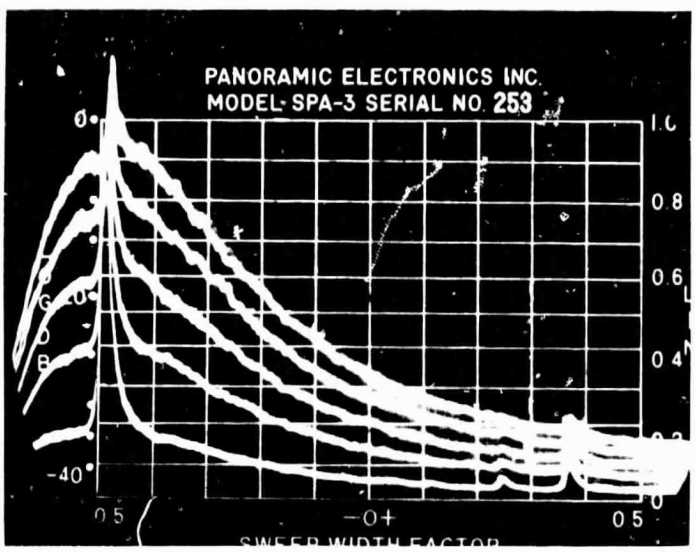


Figure 4-27: Noise Spectrum of the Detector for Various Bias Currents with Local Oscillator Off - Bias Current 3.7 milliamps, Top Trace/Bias Current 0.6 milliamps, Bottom Trace - Dispersion 1 MHz full scale; 12 db Attenuation - Two Signals at Right are Local Radio Stations.

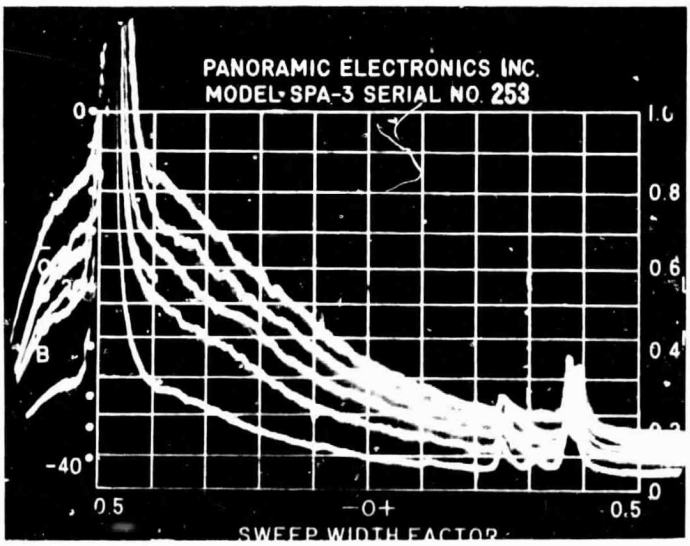


Figure 4-28: Noise Spectrum of the Detector for Various Bias Currents with Local Oscillator Power of 11.5 milliwatts - Bias Current 4.5 milliamps, Top Trace/ Bias Current 1.1 milliamps, Bottom Trace - Dispersion 1 MHz full scale; 6 db Attenuation - Two signals at Right are Local Radio Stations.

The wind tunnel must provide variable known air velocities approximately of the same magnitude as typical atmospheric winds.

With these considerations in mind, a short study was made for the design of such a wind tunnel, and a search was made for the possible manufacturers of such a tunnel.

Aerolab Supply, Inc. run by Professor A. W. Sherwood, had a prototype smoke tunnel similar to what we needed. In accordance with Professor Sherwood's existing prototype and with our particularized needs, we jointly designed a smoke tunnel which was then constructed by Aerolab.

In particular, the input plenum of the smoke tunnel contains a "honeycomb" structure with layers of fine mesh screening to reduce turbulence levels at the test section to about 1/4%.

The test section is 10" x 13" x 2-1/2" high with Kodak Irtran II windows to allow CO_2 laser radiation to enter and exit. The 1" x 4-1/2" windows are moveable along the side of the test section to allow for different incident angles of the laser beam. The windows are anti-reflection coated at 10.6μ.

An adjustable opening at the exit plenum allows for variable air velocity from approximately 0 to 30 feet per second. A small 1/8" pitot tube of Prandtl design, and an inclined manometer are used to measure the air velocity.

Smoke is generated when liquid smoke is in contact with a heating element operating at approximately 450^{o}F. The liquid smoke, obtained from Azo Industries, Inc. and similar to liquid smoke used in toy trains, is introduced into the heating element a drop at a time.

From the enclosure containing the heating element, the smoke is introduced to a smoke rake through plastic tubing. A slight positive pressure is maintained in the heating element enclosure by coupling the enclosure with the head pressure of the fan that drives the wind tunnel at the output plenum. By means of a valve,

the positive pressure in the heating element enclosure may be varied, thus varying the rate of introducing smoke into the wind tunnel, and thus controlling the density of particle contaminate in the wind tunnel. The rate of introducing smoke into the wind tunnel may further be controlled by controlling the rate of flow of liquid smoke to the heating element.

Two smoke rakes are presently in use, one which delivers the smoke in several discreet tubules of about 1/8" diameter, and another which delivers the smoke in a continuum throughout the test section. Though the continuum smoke rake more closely simulates atmospheric conditions, the discreet smoke rake is useful in gathering quantitative information, as the smoke bundles may be varied by integral numbers and the specific geometry of the system is well known.

The exhaust plenum of the smoke tunnel is attached to a large flexible hose leading outside of the building for evacuating the smoke and/or other contaminating particle agents introduced into the wind tunnel.

Using the experimental setup shown in Figures (4-29) and (4-30), the smoke generator valve was opened for a few seconds. Initially, a very large Doppler signal was observed (Figure 4-31); then, as the smoke decayed, the Doppler signal decreased as shown in Figure (4-32). This picture was taken about ten minutes after the smoke generator was turned off. The Doppler is due to smoke in the laboratory resulting from leaks in the wind tunnel and from cigarette smoke. This residual smoke has a very low density and cannot be seen with the eye.

After a period of about fifteen minutes, the air conditioner removed this residual smoke and the Doppler signal disappeared. The density of smoke particles at the time the signal becomes lost in the noise was not measured since particle counting equipment was not available.

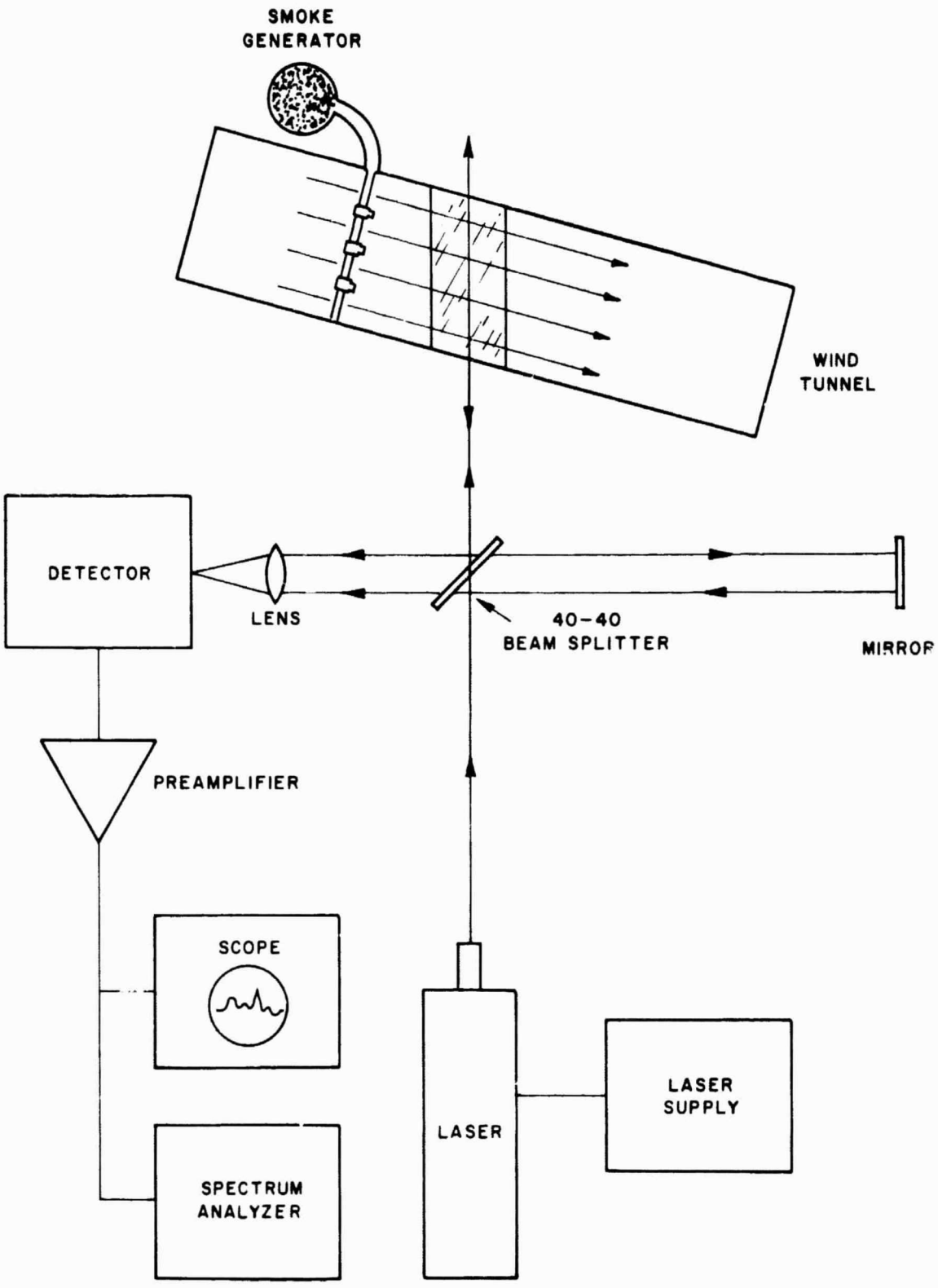


Figure 4-29: Experimental Arrangement for Wind Tunnel Tests

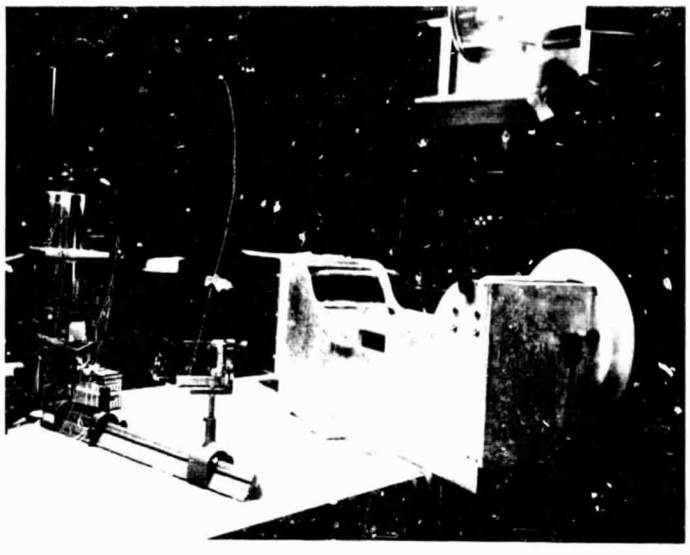


Figure 4-30: Wind Tunnel

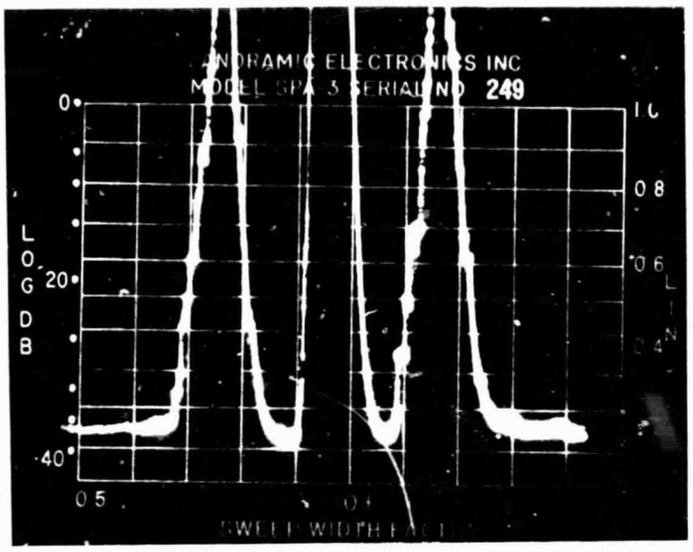


Figure 4-31: Doppler Returns from High Smoke Concentration in Wind Tunnel - Velocity Dispersion - 0.25 meter/second/division

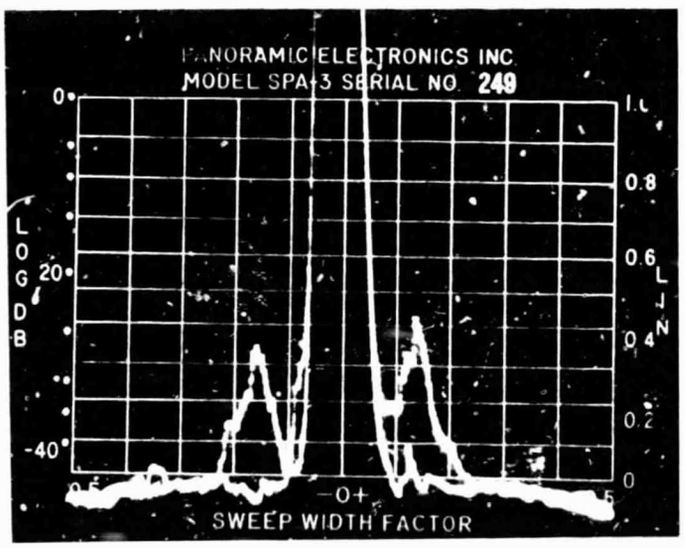


Figure 4-32: Doppler Returns from Very Low Smoke Concentration in Wind Tunnel 10 Minutes after Smoke was Turned Off - Velocity Dispersion = 0.25 meter/second/division

Figures (4-33) and (4-34) show how the Doppler velocity changed as the angle of the wind tunnel was varied. In this case, the air speed in the tunnel was one meter per second. With a scale of 50 kHz per division, we see that the displayed Doppler velocities are .50 m/sec and .37 m/sec and agree respectively with the cosines of the measured angles; i.e., with cos 60° and cos 68°.

The large signal between the Doppler sidebands is a property of the spectrum analyzer. The faint signals are due to screen persistence and the lower trace in Figure (4-32) is a double exposure which compares the residual noise and the Doppler signal. The noise spectrum was obtained by taking a picture with the signal beam blocked.

Figures (4-35), (4-36) and (4-37) show Doppler returns from the wind tunnel as the velocity of the air was reduced in three steps of 0.5 m/sec, 0.43 m/sec, and 0.31 m/sec. The amplitude does not remain constant because the smoke from the smoke generator was allowed to decay. In this case, the wind tunnel is at an angle of 60° to the signal beam. The width of the Doppler signal of about 50 kc, or the equivalent velocity spread of $\pm$.1 m/sec, is primarily due to turbulence in the wind tunnel.

4.3 Summary

Doppler heterodyne detection experiments at 10.6 microns conducted on soft targets out-of-doors verified the feasibility of the technique for a variety of systems applications. The characteristic curves of a copper-doped germanium detector were measured. These curves indicate that a maximum heterodyne current responsivity should occur at high local oscillator power and high bias voltage. Preliminary measurements were carried out on detector noise and coherence areas which will eventually lead to a determination of optimum conditions for a maximum signal-to-noise ratio for heterodyne detection at 10.6 microns.

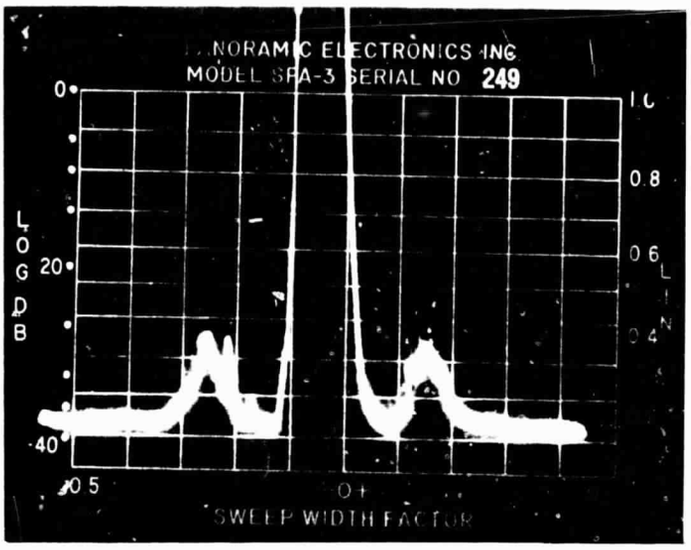


Figure 4-33: Doppler Returns from Wind Tunnel - Velocity Dispersion = 0.25 meter/second/division
$\theta = 60^{\circ}$ Angle Between Laser Beam and Wind

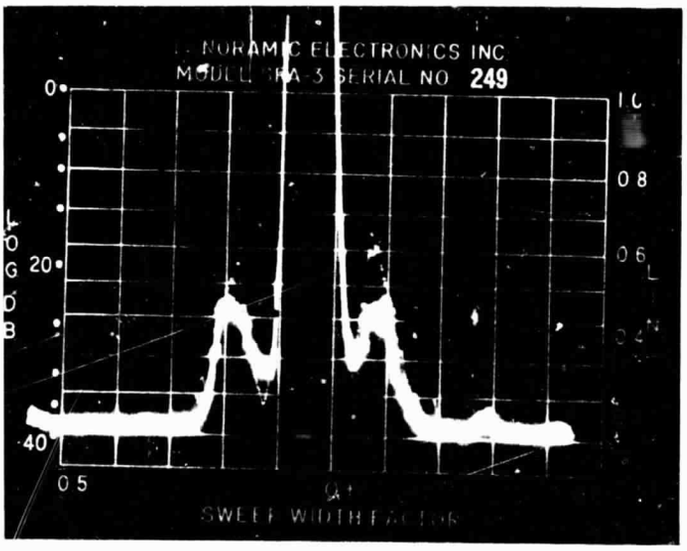


Figure 4-34 : Doppler Returns from Wind Tunnel - Velocity Dispersion = 0.25 meter/second/division
$\theta = 68^{\circ}$ Angle Between Laser Beam and Wind

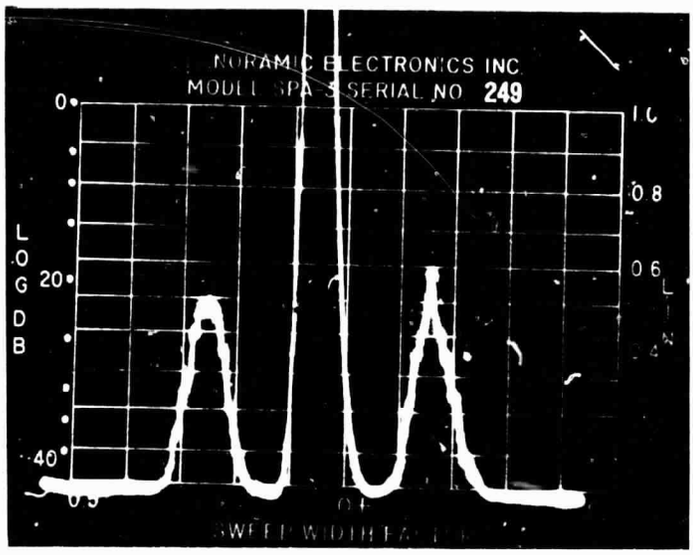


Figure 4-35: Doppler Returns from Smoke in Wind Tunnel - Velocity Component Parallel to Laser Beam = 0.5 meter/second - $\theta = 60^{o}$

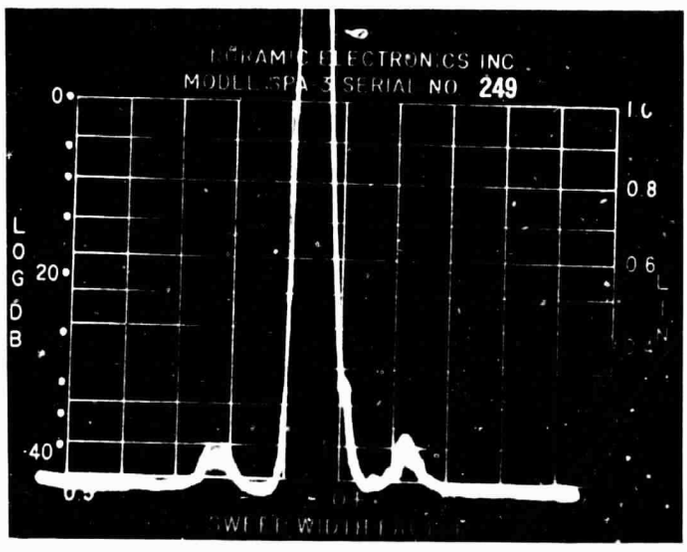


Figure 4-36: Doppler Returns from Smoke in Wind Tunnel - Velocity Component Parallel to Laser Beam = 0.43 meter/second - $\theta = 60^{o}$

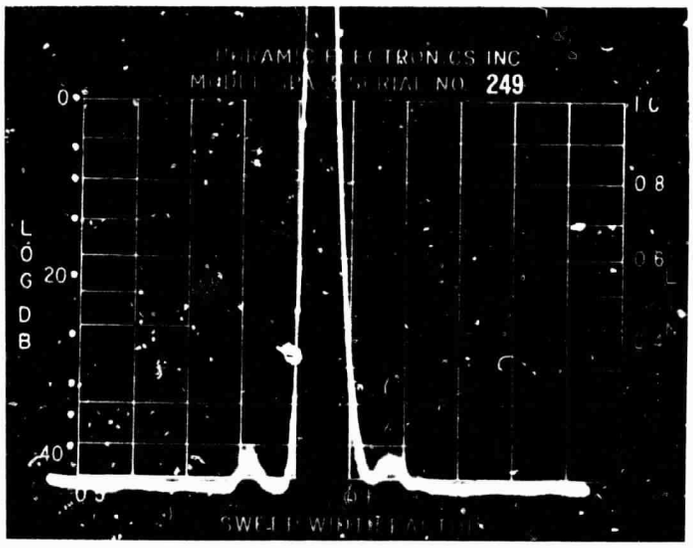


Figure 4-37: Doppler Returns from Smoke in Wind Tunnel - Velocity Component Parallel to Laser Beam = 0.31 meter/second - $\theta = 60^{o}$